universität wien

MASTERARBEIT | MASTER'S THESIS

Titel | Title

Numerical simulation of Escherichia Coli bacteria under strong confinement

verfasst von | submitted by

Selma Maria Köhler BSc

angestrebter akademischer Grad | in partial fulfilment of the requirements for the degree of

Master of Science (MSc)

Wien | Vienna, 2026

Studienkennzahl lt. Studienblatt | Degree programme code as it appears on the student record sheet:	UA 066 876
Studienrichtung lt. Studienblatt | Degree programme as it appears on the student record sheet:	Masterstudium Physics
Betreut von | Supervisor:	DI Dr. Andreas Zöttl Privatdoz.

Zusammenfassung

Escherichia coli (kurz: E. coli) gehören zu den häufigsten Bakterien der Welt. Sie bewegen sich effizient auf Oberflächen, und sind besonders effektiv darin, schmale Kanäle zu infizieren. Sie verursachen bis zu drei Viertel der Harnwegsinfektionen (UTIs), besonders solche, die innerhalb von Gesundheits- und Pflegeeinrichtungen im Zusammenhang mit Kathetern entstehen. Obwohl viele Faktoren die Populationsdynamik und Kinematik von *E. coli* beeinflussen, und das Gebiet aktiv und aus vielen Perspektiven beforscht wird, sind einige Phänomene nach wie vor kaum verstanden. Diese Masterarbeit wurde insbesondere durch eine experimentelle Beobachtung aus dem Jahr 2008 motiviert, die zeigte, dass *E. coli* unter starker räumlicher Einschränkung ihre üblicherweise bevorzugte Schwimmrichtung invertieren. Mithilfe eines einfachen Modells von scheibenförmigen Mikroschwimmern in unendlich langen, schmalen Kanälen reproduzieren wir diesen Effekt und versuchen, ihn zu erklären, indem wir die Ergebnisse mit theoretischen Modellen und experimentell gemessenen Trajektorien vergleichen. Dafür dürfen wir mit Experimentalphysikern der ESPCI Paris, besonders mit Peixin Zhang und dem Team von Anke Lindner, kollaborieren. Gemeinsam konzentrieren wir uns auf die Dynamik der Bakterienbewegung in den Kanalecken und die anfängliche Zellverteilung, während wir verschiedenste Parameter variieren. Wir stellen fest, dass die Rand-Schwimmdynamik von *E. coli* im Wesentlichen durch die Geometrie bestimmt wird: durch das Verhältnis zwischen ihrem Schwimmradius und der Kanalbreite.

Abstract

Escherichia coli (*E. coli*) are among the most common bacteria in the world. They move efficiently on surfaces and in confined geometries, such as medical catheters. They cause a large fraction of urinary tract infections (UTIs), accounting for up to three-quarters of reported cases. While many factors influence the population dynamics and kinematics of *E. coli*, some phenomena remain poorly understood. This Master's thesis was motivated specifically by a 2008 experimental observation that *E. coli* reverse their usual preferred surface swimming direction under strong confinement. Using a simple model of disk-shaped microswimmers in infinitely long, narrow channels, we reproduced this effect in simulations. Thanks to our colleagues, Anke Lindner's Team at ESPCI Paris, and especially Peixin Zhang, we could compare our results with theoretical models and experimentally measured trajectories. We focused on edge-attachment dynamics and initial cell distributions while varying confinement parameters. We found that *E. coli* edge-swimming dynamics are governed mainly by geometry: the relationship between their swimming radius and the channel width.

Contents

1 Introduction

Escherichia coli (in short, *E. coli*) is, by far, the most studied type of bacterium, with over a fifth of publications on microorganisms devoted to it [1]. The reasons for this are obvious: they are widely available, as they are present in the intestinal digestive tract of most warm-blooded species [2], as well as in water and all kinds of biological matter [3]. Furthermore, their robustness and high multiplication rate [4] on several types of cultivation media make them a perfect model organism.

Typically, *E. coli* is non-pathogenic and can even be a benefactor to our digestive functionality [3]. However, several strains can also be classified as pathogens. The majority are enteropathogenic strains that attack and occupy epithelial tissue in the intestine [5]. As for uropathogens, e.g. pathogens that infect the urinary tract, *E. coli* is by far the most common [6]. Three-quarters of uncomplicated infections and 65% of complicated infections are caused by uropathogenic *E. coli* bacteria [7], as can be seen in figure 1.1.

With an estimated 400 million cases of urinary tract infections and 230,000 associated deaths worldwide in 2019 [8], and catheter-induced urinary tract infections (CAUTIs) being the most frequent nosocomial infection [9, 10], the significance of uropathogenic *E. coli* (UPEC) for healthcare systems around the world is indisputable.

Since multi-drug resistance has become a major problem in respect to the treatment of hospital-acquired bacteremia [7], it is becoming increasingly important to prevent bacterial infections instead of treating them with broadband antibiotics as they happen.

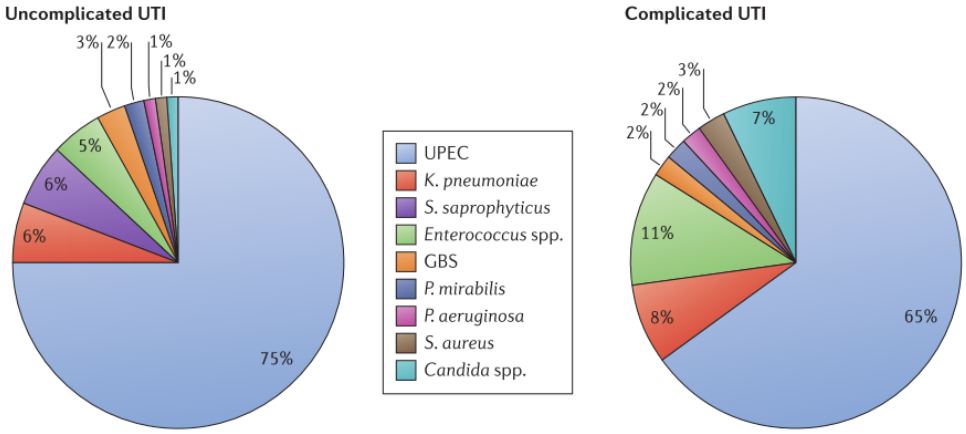

Figure 1.1: The overwhelming majority of urinary tract infections (UTIs), both complicated and uncomplicated, are caused by E. coli. Graphic taken from reference [7].

The question that arises is: what renders *E. coli* so efficient at colonizing abiotic surfaces and,

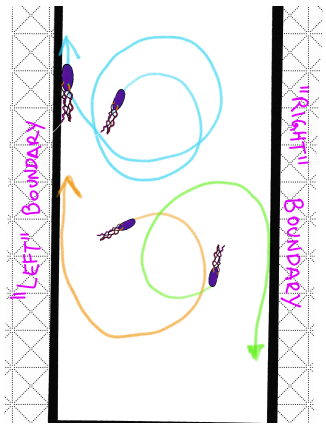

Figure 1.2: What we would expect to happen for circling bacteria - swimming along the walls of a channel in the direction of their circling motion. But sometimes, they do the exact opposite.

in particular, catheters?

The motility of various *E. coli* strains has been investigated for decades by both physicists and microbiologists. These microorganisms operate in a low-Reynolds-number hydrodynamic regime, in which inertial effects are negligible and viscous forces dominate. Under such conditions, locomotion is nontrivial: cells must exploit or overcome viscous forces and diffusive transport. The development of robust propulsion mechanisms and chemotaxis are therefore a determining factor for evolutionary fitness and survival [11]

Swimming *E. coli* are equipped with helical flagella, which are connected to the cell body via short, curved "hooks". Coordinated rotation of these flagella, driven by torque-generating molecular motors embedded in the cell membrane, produces a net force that propels the bacterium forward [12]. Due to steric interactions and the resulting force-dipole flow field hydrodynamically "traps" cells at nearby boundaries, where the torque arising from flagellar rotation induces characteristic near-surface rotational trajectories [12–14].

These motion patterns have been extensively characterized and are frequently modeled using active Brownian “circle swimmer" frameworks. Especially certain movement characteristics which *E. coli* exhibit under strong confinement are counterintuitive and remain incompletely understood [14, 15].

The initial motivation to investigate bacterial motility patterns under strong confinement in greater detail is a paper by DiLuzio et al. (2005), reference [15]. A naive expectation would be that bacteria circling in a surface would swim preferentially in the direction that matches their intrinsic sense of rotation as soon as they get "trapped" at a channel edge or crevice. When observed from the bottom of a surface, *E. coli* typically follows clockwise circular trajectories. A simple schematic (figure 1.2) illustrates this intuitive scenario, in which bacteria would be expected to migrate "upward" along the "left" boundary and "downward" along the "right" boundary. Experimental observations, however, reveal that this is not the case: instead, the cells efficiently migrate in the opposite direction [15].

In this Master’s thesis, I investigate the locomotion of *E. coli* under confinement by employing a simplified numerical microswimmer model and performing a quantitative analysis of the

resulting simulated trajectories and statistics. The numerical results are systematically compared with experimentally obtained data and analytical predictions provided by our collaborators at ESPCI Paris.

Furthermore, we aim to evaluate possible adaptations of the model by varying parameters to assess the validity and limitations of the model. This, in turn, allows for a critical evaluation of which modifications or extensions of the modelling framework could improve its descriptive and predictive accuracy.

2 Biological and theoretical background

2.1 Biological "hardware" of peritrichous *E. coli*

2.1.1 Cell geometry and structure

E. coli are Gram-negative bacteria, which means that their cell envelope consists of an outer lipopolysaccharide membrane, a peptidoglycan cell wall, and an inner cytoplasmic membrane [16]. Gram-negative bacteria frequently exhibit resistance to commonly used antibiotics, rendering them a major global public health concern [17]. *E. coli* occur naturally in gastrointestinal tracts of all warm-blooded animals [2]. They are continuously excreted into the environment, leading to their presence on a wide range of surfaces. Their ubiquity, combined with a short division time of approximately 20 minutes under optimal growth conditions [18], has contributed to their status as one of the best-characterized microorganisms. Since the 1960s, they have become the archetypal model organism in microbiology and molecular biology [3] As illustrated in Figure 2.1, *E. coli* cells exhibit a prolate, rod-shaped (bacillary) morphology. Cell dimensions can vary depending on environmental conditions such as nutrient availability; however, typical cells have a diameter of less than 1 μm and a length of approximately 2 μm [3, 18].

2.1.2 *E. coli*'s movement apparatus

At these microscopic length scales, organisms suspended in an aqueous solution at room temperature operate in a low-Reynolds-number regime (see Section 2.2). In this regime, inertial effects are negligible, and all deformations and displacements are, in principle, time-reversible, which renders directed locomotion nontrivial. Motility is not necessary for survival; several bacterial strains are non-motile [20, 21]. For the sole purpose of nutrient acquisition, active movement is not strictly required, as the diffusive transport of small molecules such as glycogen is highly efficient in low-Reynolds-regimes to their high diffusivity [18, 20]. Consequently, many bacterial strains exhibit no motility.

Even so, in conjunction with chemotaxis - defined as the directed behavioral response to spatial gradients in chemical concentration - motility enables bacteria to move toward nutrient-rich and otherwise favorable environments. Bacterial motility strategies are highly diverse and encompass swarming, gliding, twitching, sliding, and darting. *E. coli* has developed the ability to swim by the means of helical extracorporeal organelles called *flagella*.

Flagella are slender, rigid, helical polymer filaments with a diameter of approximately 0.02 μm. The location and number of attachment sites on the cell body can vary among individuals. As so - called peritrichous bacteria, *E. coli* usually has multiple flagella attached to its body [22]. They can be distributed along the entire length of the cell body. Each flagellum is typically composed

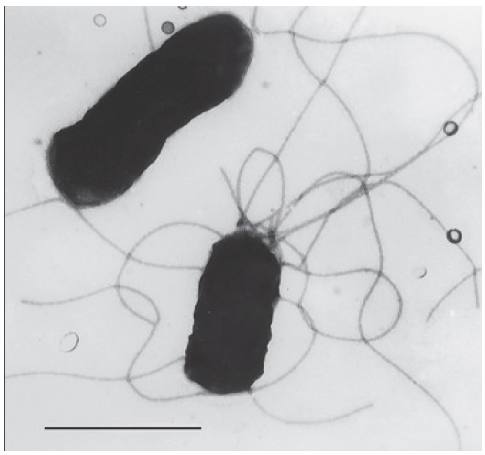

Figure 2.1: Electron microscopy image of *E. coli* showing flagella, taken from reference [19]. Scale bar: 1 μm.

of three principal structural elements: the filament, a rotary molecular motor, and a flexible hook [18].

The flagellar motor, which anchors the flagellar filament to the bacterial cell envelope, has been characterized in considerable detail. It is embedded within the cell membrane and comprises multiple structural components, including four ring complexes, a central rod, a flexible hook, and a stator unit, as illustrated in Figure 2.1. The transport of protons through the stator complex generates a torque on the C-ring, which is subsequently transmitted to the filament via the connecting rod and hook. Rotation frequency is not fixed and can vary as a function of parameters, such as the viscosity of the suspending medium, the concentration of dissolved oxygen, temperature, and other environmental factors [24]. Frequent values in literature, however, are between 100 and 150 Hz [12, 20, 22, 24] . The conformation of the C-ring is sensitive to changes in molecular concentration in the bacterium's surroundings, enabling reversible switching of the direction of rotation of the flagellar motor [23]. This bidirectional capability is the main mechanism enabling the bacteria to perform chemotaxis, as it allows the cell to reorient its trajectory in response to external stimuli.

The flagellar filaments themselves are left-handed helical structures with a pitch of approximately 2.3 μm, a contour length of up to 10 μm, and a radius of approximately 100 nm [23]. Although they are predominantly left-handed, they can undergo multiple polymorphic transitions, adopting coiled, semicoiled, or curly conformations [24]. During uninterrupted linear swimming, individual flagella form a coherent bundle that rotates in the counterclockwise direction if viewed from behind [23]. Thereby, they exert a torque on the bacterial cell body. As the bacterium is modeled as a force- and torque-free object, the cell body has to counterrotate to balance out the torque created by the rotating flagellar bundle. Owing to the substantially larger size and mass of the cell body, this counter-rotation occurs at a significantly lower angular velocity [25]. This rotation and counterrotation results in specific kinematic behaviors, particularly in the presence of boundaries or obstacles, such as a circling motion on surfaces. The reasons for this are discussed in greater detail in Section 2.2. The architecture and handedness of the flagella, together with spontaneous changes in flagellar helicity, are fundamental for

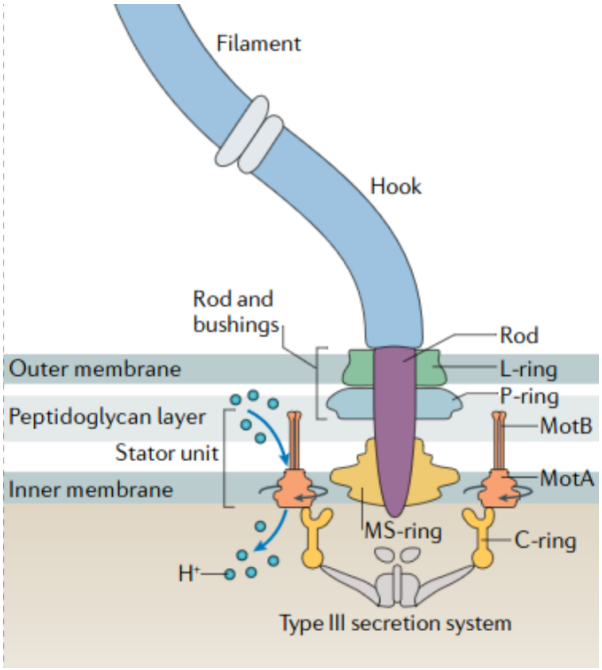

Figure 2.2: Construction of the bacterial flagellar motor. Graphic taken from reference [23]

.

determining bacterial motility patterns.

2.1.3 Chemotaxis

Like most phenotypic traits, active propulsion reflects an evolutionary advantage. A common view is that bacteria, like many macroscopic organisms, “forage" for nutrients and that motility evolved because it lets them “cover more ground." Yet, as mentioned before, small molecules diffuse efficiently on microscopic scales. Even non-motile bacteria experience a steady diffusive flux of nutrients to their surface—and many non-motile microorganisms (including some *E. coli*) survive [26].

For a spherical bacterium fixed in a uniform concentration field, the diffusive influx of a nutrient is $4\pi RND$ molecules/s, where R is the cell radius, N the bulk concentration, and D the diffusion coefficient. To raise its uptake rate by 10% solely by translating through a homogeneous medium, the bacterium would need a speed $v_0 = 1.4D/R$, which for *E. coli* is about $700\ \mu$m/s —far above physiologically attainable values [20].

Instead, bacteria can increase nutrient acquisition by moving toward higher solute concentrations. This underlies their ability to sense and respond to chemical gradients, which is a phenomenon known as *chemotaxis*. Swimming must still be fast enough to outperform diffusion: v_0 must exceed the characteristic diffusive displacement over relevant time scales. For the parameters of *E. coli* in aquaeous solution, this threshold would be about 25–30 μm/s according to theoretical considerations. This is, in fact, close to experimentally measured swimming speeds.

Peritrichous bacteria such as *E. coli* detect and respond to environmental chemical gradients,

migrating toward more favorable conditions [19, 27]. Their chemotactic signal-transduction pathways are relatively well understood. Cells sense temporal changes in stimuli via a canonical two-component system, which adjusts the probability of clockwise (CW) rotation of the flagellar motors by regulating specific proteins [28]. In turn, cells modulate their characteristic run-and-tumble behavior to bias motion in the desired direction.

2.1.4 Run and tumble dynamics

The average number of flagella per individual *E. coli* cell is reported in the literature to range between 4 and 7 [18, 29]. During forward swimming, the flagellar filaments rotate in a counterclockwise (CCW) direction (as viewed from behind the cell) [18]. The "bundling" of flagella exhibited during runs, which was mentioned previously, is a result to their left-handed helical structure. As a result, a smooth, directed propulsion is generated, despite each filament being driven by an independent rotary motor - as long as they all rotate in CCW direction. As described above, these rotary motors can stochastically reverse their direction of rotation in response to the local chemical environment of the cell.

Upon such a reversal, the previously stable flagellar bundle unravels. The filaments undergo conformational changes, individual flagella leave the bundle, and their orientations become uncorrelated. This leads to a reorientation of the entire bacterium. This reorientation "event" is called a *"tumble."* When the motors subsequently switch back to CCW rotation, the filaments return to their normal waveform, re-bundle, and the cell resumes a directed *"run"*. An entire run–tumble sequence is illustrated schematically in Fig. 2.3. Run-and-tumble behavior has been extensively studied and characterized [30], particularly in the context of bacterial chemotaxis in spatial chemical gradients [29, 31] using several different kinds of experimental setups.

Run durations and tumble frequencies have been extensively studied under a wide range of experimental conditions, and still remain an active area of research. Historically, the distribution of run times has been modeled as exponential [18]. Korobkova et al., however, quantified the durations of counterclockwise (CCW) rotation intervals of flagellar stator motors and observed that these intervals are more accurately described by a broad power-law distribution [33], which can be expressed as

$$\Psi_{PL}(t) = \frac{\gamma}{\tau_0 \left(1 + t/\tau_0\right)^{\gamma+1}}. \tag{2.1}$$

An experimental study by Figueroa-Morales et al. [34]investigated how *E. coli* bacteria can migrate upstream along crevices despite run-and-tumble dynamics. The authors performed experiments in narrow microfluidic channels under imposed flow and measured the resulting upstream bacterial contamination. These measurements were compared with microswimmer simulations.

Using the commonly cited exponential distribution of run times, the simulations failed to reproduce the experimental contamination levels. The authors therefore considered the power-law distribution of run times from equation 2.1, for which the mean run time is given by $\tau_{\text{run}} = \tau_0/(\gamma - 1)$ with $\tau_0 = 1$ s and $\gamma = 1.2$. Implementing this distribution in simulations led to

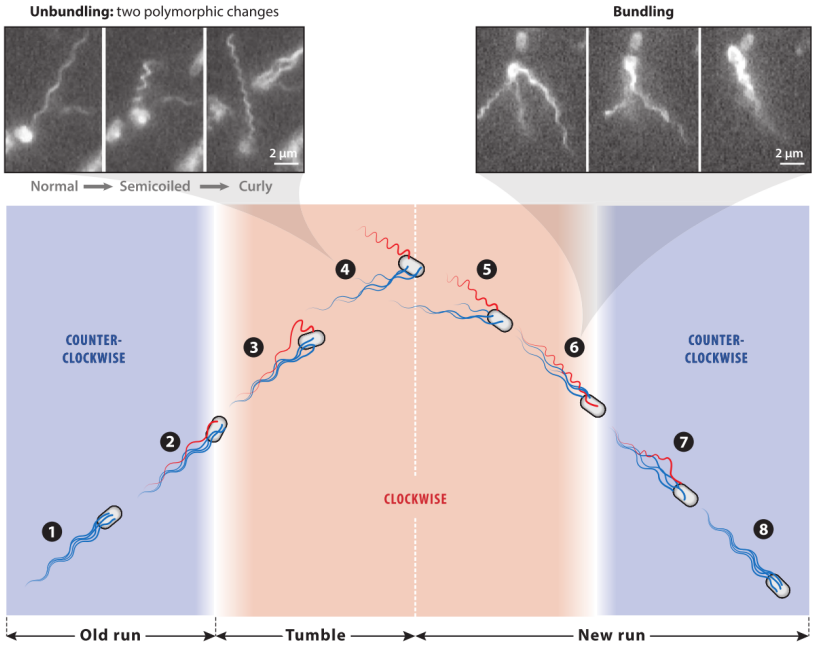

Figure 2.3: The relationship between molecular motor rotation direction and polymorphic transformations of filaments in run-and-tumble motion. Graphic taken from reference [12, 32]

substantially improved agreement with the experimental observations. Based on this result, the authors concluded that run-and-tumble statistics are a key factor governing bacterial transport and contamination in narrow channels [34].

2.2 The physics of swimming *E. coli*

2.2.1 The challenges of swimming in low-Reynolds number environments

As mentioned above, *E. coli* is a small and light organism with a characteristic cell body length of around 2 μm. To explain the physical constraints and challenges associated with locomotion at this scale, it is necessary to introduce several concepts that are fundamental to not only *E. coli* locomotion, but many biophysical mechanisms and concepts.

Reynolds number

An object moving through a viscous medium experiences *viscous drag*, which effectively represents the frictional interaction between its surface and the surrounding fluid molecules. The dimensionless ratio that characterizes the relation between viscous forces and inertial forces for an object of characteristic size a, traveling at speed v in a fluid of density ρ and dynamic

viscosity μ, is known as the **Reynolds number**. It is defined as

$$Re = \frac{\text{inertial forces}}{\text{viscous forces}} = \frac{av\rho}{\eta} \tag{2.2}$$

To assess the relevance for *E. coli*, consider an idealized disk-shaped bacterium with a diameter of 2 μm swimming at about 30 μm s^{-1} in water at room temperature [18, 20]. Water is one of the least viscous common liquids, with a dynamic viscosity of $\mu_{\text{water}} \approx 10^{-3}$ Pa s at 20°C [35]. By definition, all physical units cancel in the calculation of the Reynolds number Re. For *E. coli* in water, using equation 2.2, Re is on the order of 10^{-4}, whereas for a human swimming in a pool it is typically on the order of 10^4.

What are the implications of operating in the low-Reynolds-number regime, $Re \ll 1$, for an individual organism? For a motile organism, locomotion can be realized either by taking advantage of external hydrodynamic conditions, such as background flows or currents, or by performing body deformations that drive active propulsion. To achieve self-propelled swimming, an organism must deform its body or appendages in a periodic or cyclic fashion. In fluid environments characterized by $Re \gg 1$, inertial effects dominate, and the associated mechanics of motion are relatively intuitive. For example, a human swimmer can passively coast several meters between breaststrokes. At the onset of every subsequent stroke, the swimmer has already achieved a substantial spatial displacement during the gliding phase, and starts the next stroke from an advanced position.

In the regime $Re \ll 1$, inertial contributions become negligible and viscous forces dominate the dynamics. Consider, for instance, a bacterium swimming at 30 μm s^{-1} in water, as mentioned in the introduction of this section. If it were to interrupt its propulsive activity instantaneously, it would coast a distance of only $\sim (0.1$ Å) before coming to rest within approximately 0.3 μs. This hydrodynamic regime is can be compared to that of a human attempting to swim in high-viscosity fluid, like molasses, and not being able to perform movements faster than 1 cm min^{-1} [20]. With inertia therefore being irrelevant, we recall the famous Navier-Stokes equation 2.3:

$$-\nabla p + \eta \nabla^2 = \rho \frac{\partial \vec{v}}{\partial t} + \rho(\vec{v} \cdot \nabla)\vec{v} \tag{2.3}$$

Since we have calculated that inertial effects become irrelevant, we can eliminate all inertial terms in the equation. $\eta \nabla^2 \vec{u} = \nabla p$ remains, where p denotes the pressure, and the Stokes equations become kinematically reversible: the direction and “rate" of time become irrelevant, and any flow is invariant under time reversal. Consequently, if an organism executes a sequence of shape deformations and subsequently retraces that sequence in reverse order, it will return precisely to its initial position. This would represent a closed loop in configuration space. Any such deformation cannot produce a net displacement of the organism in low-Reynolds regimes. This principle is known as the *scallop theorem*: a simple organism possessing only a single degree of freedom—such as a scallop with one hinge-like joint—cannot achieve locomotion in a purely viscous, low-Reynolds-number environment. Hence, more sophisticated strategies for propulsion must be employed.

For *E. coli*, this constraint is overcome through the rotation of helical flagellar appendages, which constitutes a non-reciprocal trajectory in configuration space [20].

2.2.2 Hydrodynamics of rotating flagella - what makes *E. coli* swim

We recall that during runs, flagella bundle together [12] and can effectively approximated as one helix. Since bacterial swimming fluid motion occurs at Reynolds number regimes far smaller than 1 ($Re \simeq 10^{-4}$), fluid dynamics are entirely governed by Stokes flow, which means that all nonlinear components in the hydrodynamic equations are irrelevant [36]. The propulsion force F_{thrust} and the torque N_{fl} acting on the flagella is therefore:

$$-F_{thrust} = Av - B\omega \tag{2.4}$$

$$N_{fl} = -Bv + D\omega \tag{2.5}$$

In this equation, v denotes the propulsion speed of the bacterium, typically reported in the range of 20–$30\ \mu$m/s [12, 18]. The angular velocity ω [rad/s] describes the rotation of the flagellar bundle, which is later related to the trajectory curvature and swimming radius of the bacterium. Because of the linear nature of their relationship, the coefficients A, B and D can be written as a linear Propulsion matrix P. [20, 36]:

$$P = \begin{bmatrix} A & -B \\ -B & D \end{bmatrix} \tag{2.6}$$

It can be proven that the off-diagonal elements must be equal and the flagellar propulsion matrix must be symmetrical [20]. As the helix rotates, each material element moves with a local velocity relative to the surrounding fluid. This velocity can be decomposed into components parallel and perpendicular to the local tangent of the filament. Due to the anisotropic viscous drag experienced by slender bodies in Stokes flow, motion perpendicular to the filament generates a larger resistive force than motion parallel to it [12].

Because of the chiral geometry of the helical filament, the axial components of the local drag forces do not cancel when integrated along the flagellum, resulting in a net propulsive force along the helix axis. To explain the circular trajectories flagellated bacteria perform on surfaces, we recall that the bacterium is force- and torque-free. The torque generated by the rotating flagella is balanced by an opposite countertorque, causing the cell body to rotate in the opposite direction. Due to the much larger mass and drag of the cell body compared to the thin flagellar filaments, this counterrotation occurs at a substantially lower frequency.

The sketch 2.4 below shows the torque created by the rotation of the flagella and the counter-torque acting on the bacterium's body. The horizontal vectors represent the forces, which cause the bacterium to swim in the direction of its cell body.

Figure 2.4: Sketch from reference [12], showing torques and forces acting on a bacterium during rotation of helical flagella.

2.2.3 Cell dynamics on surfaces

Figure 2.4 illustrates the forces and torques acting on the cell body. During free and unconfined swimming, the propulsion force results in a relatively straight trajectory under the influence of diffusion. We now consider the top view of a cell swimming on a no-slip boundary. We can see the torque generated by the rotating flagella and the resulting counter-rotation of the cell body will result in a change in direction, i.e. impose a certain added angular velocity on the bacteria's orientation. The schematic representation in Figure 2.5 shows how the torque resulting from the rotation of the flagella and the countertorque from the cell body cause the bacterium to rotate. The superposition of this rotational motion with the propulsion kinematics leads to characteristic circular trajectories near surfaces. This phenomenon has been observed in multiple experiments and publications, and occurs on several different no-slip surface types [37].

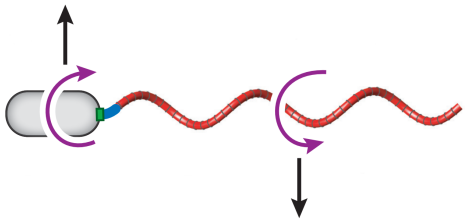

Figure 2.5: Schematic description of the torques acting on a swimming cell on a surface, causing a rotating motion, and, in turn, circular trajectories. Figure adapted from reference [12]

Figure 2.6 presents an example of experimentally observed bacterial behavior at a solid–liquid interface. Upon approaching the surface, individual bacteria make contact, attach, and subsequently start performing circular trajectories on the surface. For bacteria with left-handed flagella, the swimming trajectories are predominantly oriented in the clockwise direction [14].

2.2.4 Wall and surface alignment

The phenomenon that cells accumulate on surfaces, and especially in channel edges and crevices, has been repeatedly observed by experimentalists since the mid-20th century [14, 39–41]. This accumulation was long attributed primarily to hydrodynamic interactions. However, at distances of more than only a fraction of a bacterial cell length from the wall, the dynamics are already strongly influenced and effectively dominated by fluctuations and Brownian motion [12, 37]. Simulations using the simplified model of self-propelled spheres, in reproduce similar wall accumulation patterns [13, 42]. Therefore, we conclude that the accumulation of bacteria at boundaries stems mostly from statistical and steric mechanisms, but are further enhanced by hydrodynamic interactions.

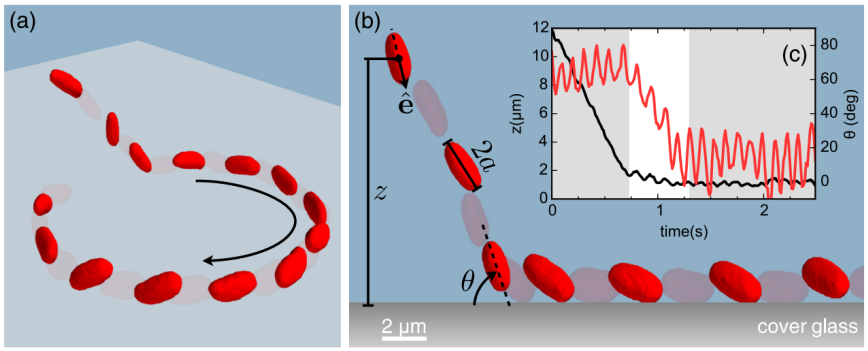

Figure 2.6: Figure taken from reference [38] with the following description: "(a) Sequence of volumetric reconstructions of swimming cells during a wall-entrapment event. (b) A close and lateral view of another cell colliding with the wall. Time intervals between reconstructions are 0.2 s in both figures. (c) For the same cell as in (b), the wall distance is plotted as a black line, while the red line plots the angle of the cell-body axis. In both curves, three stages can be identified: approach to the wall, reorientation, and surface swimming. The grey shaded areas help to visualize these three stages."

Wall alignment due to the flow-induced force dipole

In addition to the torque generated by the rotating motors, the rotation of the helix couples to the suspending fluid. As discussed in the previous chapter on low-Reynolds number hydrodynamics, viscous forces dominate in a microscale environment This dominance is relevant not only for the swimmer itself, but also for the surrounding fluid, which is also experiences drag caused by the motion of the suspended object. Thereby, a flow field is induced. Consequently, the swimming motion of the bacterium gives rise to a force dipole acting on the surrounding medium. These hydrodynamic signatures have been both experimentally measured and theoretically modeled, and the resulting flow field is illustrated in figure 2.7.

If we imagine the above picture close to a surface, a part of the force dipole field is "cut off" [12, 40, 43]. The resulting image effect leads to a net force acting on the bacteria, essentially pushing it towards the surface, as illustrated in figure 2.8.

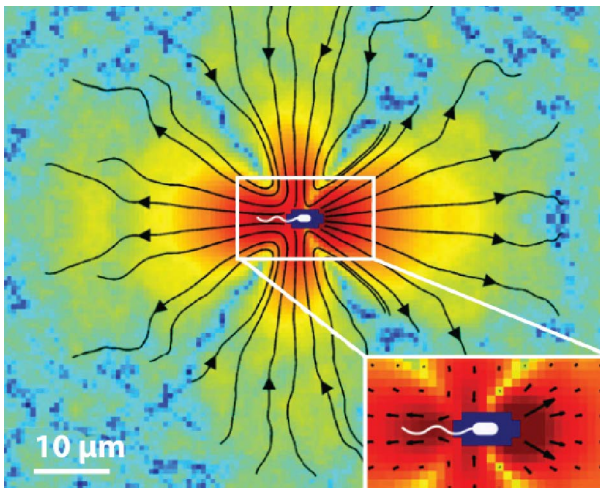

Figure 2.7: Measurement of the flow induced by swimming *E. coli*. Figure taken from reference [12]

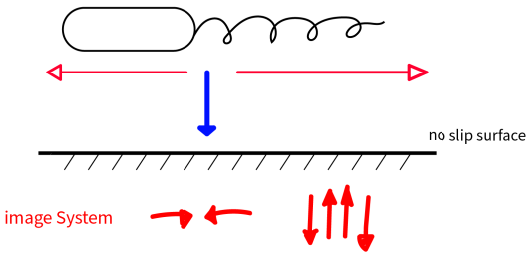

Figure 2.8: Acting forces on the real and the image system. Figure reproduced from references [25, 40]

When *E. coli* swim within approximately $1–3\ \mu$m of a solid boundary, experimental observations indicate that they can remain in the close to that surface for durations up to and even exceeding one minute [37]. They effectively become hydrodynamically “trapped" near the wall. In 2008, Berke et al. proposed a theoretical model describing the influence of hydrodynamic interactions with nearby walls on the locomotion of swimming *E. coli* cells. In this framework, they introduced a mathematical formulation for an additional rotational component, Ω_z infinite in the direction of $\vec{e}_z$, which tends to align the swimming cell with the surface. If rotation rate $\vec{\Omega}$ on a surface is expressed as a function of the vorticity of the flow field $\vec{\omega} = \nabla \times \vec{v}$ and $\vec{E} = \frac{1}{2}(\nabla\vec{v} + \nabla\vec{v}^T)$ as the rate of strain of the flow field due to the image system in the following

manner [40]:

$$\vec{\Omega} = \frac{1}{2}\vec{\omega} + \left(\frac{\gamma^2 - 1}{\gamma^2 + 1}\right) \vec{e} \times (\vec{E} \cdot \vec{e}) \tag{2.7}$$

the additional component Ω_z can be expressed as a function of the angle of the bacterium in respect to the wall, ϑ. It is defined analogously to figure 3.5, only in 3D. Using this notation, Berke et al. have obtained the following:

$$\Omega_z(\vartheta, y) = -\frac{3p \cos\vartheta \sin\vartheta}{64\pi\eta y^3} \left[1 + \frac{\gamma^2 - 1}{2(\gamma^2 + 1)}(1 + \cos^2\vartheta)\right] \tag{2.8}$$

Here, p denotes the dipole strength, and γ the shape factor of the entire cell, which for *E. coli* is $\gamma \gg 1$. Under these conditions, the wall-alignment rate Ω_z always has the same sign as $-\cos\vartheta \sin\vartheta$. The characteristic timescale on which *E. coli* cells align parallel to the wall is given by $\tau_\Omega \sim \eta L^3/p$, where L is the distance to the nearest wall [40]. However, Berke et al. report that this model overestimates cell concentrations at surfaces relative to experimental measurements. Subsequent studies further indicate that wall hydrodynamics impose only a minor influence on cell reorientation, and that this effect is significant only in the immediate vicinity of the surface [37].

Steric torque

As mentioned previously, simplified simulations that neglect hydrodynamic drag from nearby surfaces can still reproduce experimental observations reasonably well. Li and Tang (2009) showed that the so-called steric alignment torque dominates over hydrodynamic alignment in many situations [44]. The basic mechanism is briefly summarized here following their work. Note that the definition of ϑ here is defined as the angle between the velocity unit vector of the microswimmer and the surface, as can be seen in figure 2.9, and the calculations are done for a 2D x-y-plane.

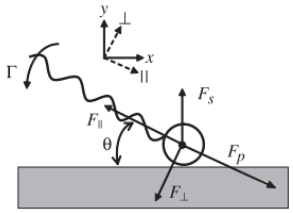

Figure 2.9: Formalism used by Li and Tang for their considerations about steric alignment torques, taken from reference [44]

When a bacterium approaches a solid boundary, steric interactions prevent motion perpendicular to the surface. Consequently, the velocity component normal to the wall vanishes. Decomposing the propulsion force generated by the flagellar bundle F_p into a component parallel to the bacterial long axis, $F_\parallel$, and a component perpendicular to it, $F_\perp$, as well as a steric

force normal to the surface F_s, one obtains a steric torque Γ that tends to align the bacterium with the surface.

The steric forces and torques associated with the velocity components of $\vec{V}$ can be written as

$$\begin{pmatrix} F_{\parallel} \\ F_{\perp} \\ \Gamma \end{pmatrix} = \begin{pmatrix} -A_{11} & 0 & 0 \\ 0 & -A_{22} & A_{23} \\ 0 & A_{32} & -A_{33} \end{pmatrix} \begin{pmatrix} V_{\parallel} \\ V_{\perp} \\ \Omega \end{pmatrix}. \tag{2.9}$$

At low Reynolds number, force balance parallel to the surface requires

$$F_p \cos\vartheta + F_{\parallel} \cos\vartheta + F_{\perp} \sin\vartheta = 0.$$

From this relation, the translational velocity along the surface and the rotation rate induced by steric interactions can be obtained as

$$V_x = \frac{A_{33} \cos\theta}{A_{33}(A_{11} \cos^2\theta + A_{22} \sin^2\theta) - A_{23}^2 \sin^2\theta} F_p, \tag{2.10}$$

$$\Omega = \frac{A_{23} \sin\theta \cos\theta}{A_{33}(A_{11} \cos^2\theta + A_{22} \sin^2\theta) - A_{23}^2 \sin^2\theta} F_p. \tag{2.11}$$

Using this formalism, Li and Tang were able to reproduce the experimentally observed accumulation of bacteria such as *E. coli* near surfaces with good agreement [44].

In our simulations, a simplified representation of this mechanism is implemented through a hard boundary condition at the channel walls, which suppresses motion normal to the surface. This effectively captures the steric alignment mechanism described above and allows the model to reproduce the characteristic surface accumulation behavior of swimming bacteria.

2.2.5 Non-continuity dynamics and Brownian noise

We have thus far examined the viscous forces acting on swimming *E. coli* cells. However, as explained in the previous chapter, there exists an additional challenge that these bacteria must overcome in order to achieve directed motion: their locomotion must outperform diffusive effects. Due to their extremely small size, the interaction of the cells with the surrounding fluid molecules can no longer be approximated as a continuous medium. Instead, they undergo discrete collisions with these molecules, resulting from thermal fluctuations, which in turn cause random displacements. Both translational and rotational diffusion occur. This phenomenon is referred to as *Brownian motion* [45]. Brownian motion arises from the stochastic interactions of microscopic objects, such as aerosols or bacteria, with the constituent molecules of the surrounding medium, and is driven by thermal agitation. When the characteristic length scale and mass of an object are sufficiently small, the spacing between solvent molecules and the magnitude of their impacts (for example, those of water molecules in an aqueous solution) become non-negligible. Consequently, the object is significantly displaced by these collisions. In the specific case of *E. coli*, it has been observed that cells undergo translational displacements

on the order of 1 μm/s and rotational reorientations of up to 30 °/s due to Brownian motion [18].

If we now combine what we have learned about all the components of *E. coli* near surfaces, we can construct the corresponding *Langevin equations of motion* 2.14 below.

$$\frac{d}{dt}\varphi(t) = \omega + \sqrt{2D_R}W_\phi \tag{2.12}$$

$$\frac{d}{dt}x(t) = v_0\cos\big(\varphi(t)\big) + \sqrt{2D_T}W_x \tag{2.13}$$

$$\frac{d}{dt}y(t) = v_0\sin\big(\varphi(t)\big) + \sqrt{2D_T}W_y \tag{2.14}$$

They describe the circular trajectories of *E. coli* on a surface in the x-y-plane, and with an orientation φ over time. ω denotes the rate of rotation caused by the interaction with the surface, and is the determining factor for the swimming radius, which will be very relevant for the outcome of our simulations. v_0 is the propulsion speed typically exhibited by *E. coli* on straight trajectories, which was measured to be between 20 and 30 $\mu m/s$ in the experiments conducted by Peixin Zhang at ESPCI Paris. Last, but very important, are the random components W_φ, W_x and W_y, which represent the random influence of Gaussian white noise. The diffusion constants for rotational diffusion D_R and translational diffusion D_T, respectively, depend mostly on thermal noise. Both of them are linear with Temperature and inversely dependent on the fluid viscosity η. For spherical particles of radius R, the diffusion constants are given by:

$$D_T = \frac{k_B T}{6\pi\eta R}\left[\frac{\mathrm{m}^2}{\mathrm{s}}\right] \tag{2.15}$$

$$D_R = \frac{k_B T}{8\pi\eta R^3}\left[\frac{\mathrm{rad}}{\mathrm{s}}\right] \tag{2.16}$$

However, for bacteria, the displacement caused by translational diffusion is comparatively small compared to the displacement caused by bacterial swimming motion [44]. The rotation diffusion coefficient, by contrast, is highly relevant for the swimming dynamics of bacteria, especially close to edges and crevices.

The relevance of diffusion effects compared to ballistic (active) swimming is characterized by the *Péclet number*. Similar to the Reynolds number, it is a dimensionless quantity that compares diffusive and advective transport processes. In this context, it can be interpreted as the ratio between the time t_D required for a particle to diffuse over its own diameter and the time t_0 required to actively swim the same distance [46]:

$$Pe = \frac{t_D}{t_0} = \frac{2Rv_0}{D}. \tag{2.17}$$

For $Pe \ll 1$, particle kinematics are largely determined by diffusion, whereas for $Pe \gg 1$ the dynamics are dominated by active swimming.

2.3 Other possibly relevant factors - biofilms, collective locomotion, and more

There are a lot more factors to consider that could potentially contribute to *E. coli*'s exceptional ability to infect catheters and cause recurrent urinary tract infections.

One is biofilm formation: motile bacteria such as *E. coli* can form biofilms on both abiotic and biological surfaces [47, 48]. External organelles like *cilia* and *pili* also show high affinity for epithelial surfaces [5], which may help explain the high recurrence of *E. coli* urinary tract infections [49].

Another relevant research direction concerns the behavior of *E. coli* in shear flows. Strong viscous shear can damage or break stiff flagella [18], while experiments also indicate that flow can stabilize bacterial motion [34, 50, 51]. Furthermore, hydrodynamic interactions arising from collective dynamics in dense bacterial suspensions may also influence transport and accumulation behavior.

There are several additional factors that may contribute to the remarkable ability of *E. coli* to infect catheters and cause recurrent urinary tract infections. However, these mechanisms remain active areas of research and lie beyond the scope of this thesis. It is nevertheless noteworthy that simplified microswimmer models are already able to reproduce key experimental observations despite neglecting many of these additional effects.

3 Methods

Working in Anke Lindner's team at PMMH (Physics and Mechanics of Heterogeneous Media) at ESPCI Paris, Peixin Zhang and colleagues conducted experiments on *E. coli* under strong confinement. The aim of this thesis is to reproduce the phenomena observed in these experiments using numerical simulations and to gain further insight into the underlying mechanisms.

First, the experimental setup is presented in order to highlight potential challenges arising from real-world conditions. Next, the simulation framework is described, including the base algorithm as well as the measurement and statistical analysis methods employed. Finally, since the goal is to compare experimental and simulation results and relate them to analytical considerations, the relevant variables and definitions used throughout this work are introduced.

AI tools, such as ChatGPT, have been used to assist with matplotlib code for data analyisis and plotting in Python, as well as phrasing throughout this thesis.

3.1 Experimental Setup

Peixin Zhang conducted the experiments to compare with our simulations. In the experiments, smooth-swimming (which means they are non-tumbling) *E. coli* strain AD63 were used. The confimement was imposed by rectangular, non-slip PDMS microchannels fabricated with widths of 20–200 μm and heights of 40–60 μm. The channels contained no imposed flow, and a dilute bacterial suspension was used to minimize swarming and collective hydrodynamics effects.

Bacteria were tracked with two methods. First, an inverted microscope observed them at the bottom surface ($z = 0$) using a 40x objective, recording at 10 fps for 50 s. The setup is sketched in figure 3.1.

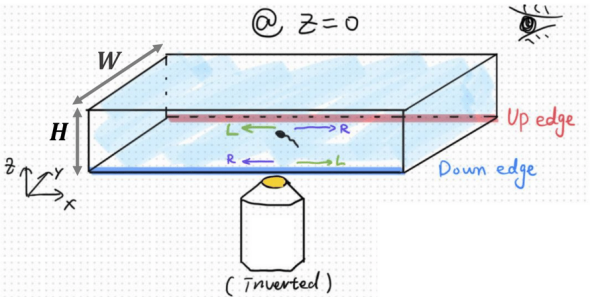

Figure 3.1: Experimental setup sketched by Peixin Zhang.

To describe the 2D bacterial dynamics at the bottom surface, a regular Eulerian coordinate system was used. In the experiment, however, the channels are horizontal, so the x and y directions are swapped relative to the laboratory frame, as shown in figure 3.2.

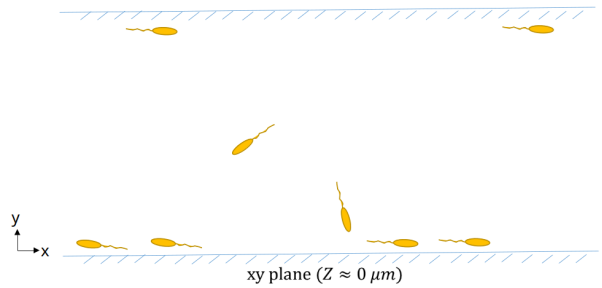

Figure 3.2: Observation frame and coordinate system by Peixin Zhang.

3.1.1 3D Lagrangian tracking

In addition to the 2D analysis, Peixin Zhang performed 3D Lagrangian tracking to investigate bacterial dynamics on all four walls of the rectangular PDMS channels. This included addressing the definition of the incoming angle by introducing trajectory “surfaces" at wall collisions (see figure 3.3).

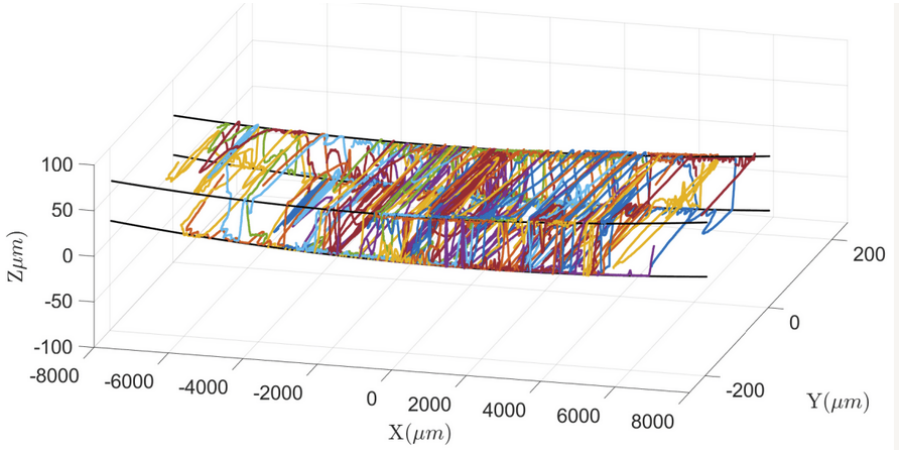

Figure 3.3: Reconstructed 3D Lagrangian trajectories of bacteria in a rectangular PDMS channel (Peixin Zhang), illustrating motion along all four walls and the trajectory surfaces used to define the incoming angle at wall collisions.

These data and the reconstructed 3D trajectories are not analyzed further in this work, but they are documented here so that we can refer to them in the subsequent discussion, particularly regarding the experimental challenges they reveal.

3.2 Simulation

3.2.1 Base model

As explained in Section 2.2, bacteria in confinement rapidly attach to surfaces and remain there for most of the time. We therefore employ a two-dimensional (2D) microswimmer model, where

the channel edges are represented as impenetrable walls. The 2D simulation plane corresponds to the bottom surface of the PDMS channel used in the experiments.

Prolate bacterial cells are approximated as spheres with a radius of $1\,\mu$m. Previous studies have shown that cell shape primarily influences the rotational diffusion coefficient D_R. In our model, we therefore use a value of D_R measured experimentally for *E. coli*.

The microswimmer model is based on empirical observations of near-surface bacterial trajectories. The Langevin equations 2.14 were discretized as follows, using vectorized NumPy operations in Python:

$$\begin{aligned} x_i &= x_{i-1} + v_0\,\cos(\varphi_{i-1})\,\Delta t + \sqrt{2D_T\,\Delta t}\,w_{x,i} \\ y_i &= y_{i-1} + v_0\,\sin(\varphi_{i-1})\,\Delta t + \sqrt{2D_T\,\Delta t}\,w_{y,i} \\ \varphi_i &= \varphi_{i-1} + \omega_0\,\Delta t + \sqrt{2D_R\,\Delta t}\,w_{\varphi,i} \end{aligned} \tag{3.1}$$

Here, x_i and y_i denote the Eulerian coordinates in [μm], and φ_i is the particle orientation in [rad] at timestep i. Since the swimming radius provides a more intuitive description of the observed swimming direction inversion, we parameterize the simulations by the swimming radius R_0. The corresponding angular velocity of the particle trajectory, ω_0, is then calculated for each simulation run from this parameter with $\omega_0 = -\frac{v_0}{R_0}$. The numbers $w_{x,i}$, $w_{y,i}$, and $w_{\varphi,i}$ are randomly and independently drawn from a Gaussian distribution, reflecting the stochastic nature of the Langevin equations.

In the simulations, the x-direction is parallel to the channel width and runs from $x = 0$ at the left wall to $x = W_0$ at the right wall. Consequently, $x \in [R,\, W_0 - R]$ during each run, where R is the radius of the swimming sphere. The walls are assumed to be infinite in the y-direction, such that $y \in (-\infty, +\infty)$. In practice, however, the displacement in y remains much smaller than $\sum_t v_0\,\Delta t$. The time step Δt (in [s]) is indexed by i. The translational and rotational diffusion coefficients are denoted by D_T (in [μm^2/s]) and D_R (in [rad^2/s]), respectively.

Each particle is assigned a unique ID (its index in the NumPy configuration array during regular steps) to facilitate subsequent analysis. In addition, a Boolean flag indicates whether the particle is currently attached to a wall, which is required to analyze attachment and detachment events and will be discussed later in this chapter.

3.2.2 Parameters

To assess the relevance of each parameter for the observed effects, the simulations were run with various sets of parameters. For the main simulations, the physical constants—the translational diffusion constant D_T, rotational diffusion constant D_R, edge interaction region ε (see explanations below), propulsion speed v_0, angular velocity ω_0, and disk radius R—were fixed and chosen close to empirical values.

As we will see, the ratio of R_0 to channel width W_0 strongly affects bacterial flux and swimming direction. Therefore, we ran simulations for each combination of these two parameters from a parameter set shown in table 3.1. The number of particles N, timestep Δt, and total runtime T

were adjusted as needed, but the main set of parameters used was:

$$R = 1\,\mu\mathrm{m} \tag{3.2}$$
$$D_T = 0.21220659\,\mu\mathrm{m}^2/\mathrm{s} \tag{3.3}$$
$$D_R = 0.057\,\mathrm{rad}^2/\mathrm{s} \tag{3.4}$$
$$v_0 = 25\,\mu\mathrm{m}/\mathrm{s} \tag{3.5}$$
$$\Delta t = 0.001\,\mathrm{s} \tag{3.6}$$
$$N = 10000 \tag{3.7}$$
$$T = 100\,\mathrm{s} \tag{3.8}$$

As discussed in the theoretical section of this thesis, the rotational diffusion coefficient D_R plays a key role in determining the kinematics of microswimmers. The corresponding *Péclet number* Pe, defined in Eq. 2.17, can be obtained experimentally by estimating the relevant diffusive and ballistic timescales, and can likewise be calculated from the parameters used in the simulations.

For a meaningful comparison between experiments and simulations, it is important that the corresponding Péclet numbers are of similar magnitude. This condition is satisfied for the parameter choices used in this work, as $Pe >> 1$ for rotational and translational diffusion coefficients.

Table 3.1: Parameter table for all values used as R_0 and W_0 parameters.

Parameter	Values [μm]
R_0	2.5, 5.0, 7.5, 10.0, 12.5, 15.0, 17.5, 20.0, 22.5, 25.0, 27.5, 30.0, 32.5, 35.0, 37.5, 40.0
W_0	10.0, 20.0, 40.0, 100.0, 200.0

To better understand the observed phenomena, we also ran a purely geometric simulation by removing noise. We used two main datasets: one with noise and one without.

3.2.3 Initial conditions

Depending on the dataset, we used two particle initialization methods. Since the channels extend infinitely along $\hat{e}_y$, the initial y-position is irrelevant, and all particles were set to $y_0 = 0$. In x-direction, x was drawn from a uniform distribution over $[R, W_0 - R]$. The initial orientation φ_0 was drawn uniformly from $[0, 2\pi)$.

Because initial orientation and x-position strongly affected the results, we implemented a second method that initializes particles from an orientation–x-position histogram. The algorithm takes a 2D array of bin edges in x and φ and either places an equal number of particles uniformly in each bin or a specified number per bin. This allows using an experimental snapshot as the initial condition for a simulation.

The number of x-bins depends on channel width, with $N_{\text{bins}} = W_0/100$. For φ, we used 10°-wide bins; within each bin, orientations were uniformly distributed, and 100 particles were initialized per bin.

3.2.4 Wall interactions

Due to hydrodynamic interactions with rigid walls, particles adhere to them and remain attached for long periods. Various models have been proposed to describe this interaction with obstacles, but the effect can be accurately captured with simple methods.

In our case, a complex potential for wall interactions was unnecessary. In the experiments, bacteria collide with walls, cannot cross them, and then swim along them for several reasons. We approximate this using an infinite potential: once the disk collides with a wall, it is reset to lie on the wall at a distance equal to the particle radius R plus a small offset $\eta = 0.1\,\mu$m.

Experimentally, bacteria attach to the wall and then swim nearly parallel to it. They stop circling, which we model by modifying the orientation update near walls, as in equation 3.9:

$$\varphi_i = \begin{cases} \varphi_{i-1} + \sqrt{2D_R\Delta t}\cdot w_{\varphi,j}, & x < \varepsilon \\ \varphi_{i-1} + \omega_0 + \sqrt{2D_R\Delta t}\cdot w_{\varphi,j}, & \varepsilon < x_i < W_0 - \varepsilon \\ \varphi_{i-1} + \sqrt{2D_R\Delta t}\cdot w_{\varphi,j}, & x > W_0 - \varepsilon \end{cases} \tag{3.9}$$

The wall interaction region ε is fixed at $3\,\mu$m for all runs. As shown in the results, this simple treatment reproduces the observations well, even though the underlying physical mechanism differs from that in the experiments.

3.2.5 Trajectory recording and statistical analysis

One major challenge for reproducibility and auditability was performing statistics on very large datasets. A single simulation run could produce up to 3×10^9 datapoints, and each parameter set required 75 runs (one for each W_0, R_0 combination), making extended post-run analysis on full datasets infeasible. We therefore focused on computing statistics during the run and storing only a few key datasets for validation.

Full trajectories are an important metric for validating bacterial motion and visually comparing with experiments, but they do not require maximum temporal resolution. Storing only a fixed number of trajectories (typically 100–1000) and recording their position and orientation every 10 timesteps was sufficient for this first validation step.

To facilitate reproducibility, the initial particle conditions were stored at $t = 0$ as a snapshot of the entire configuration space in a numpy `.npy` array. This file loads quickly, can be reused for runs with different parameters, and was later used to analyze particle behavior after initialization.

Intra-run statistics

Statistics requiring large, precise datasets were computed during the simulation. We focused on the probability density in the x-direction $P(x)$, the velocity in the y-direction v_y, and the particle flux $j_y(x) = P(x)\,v_y(x)$. For these quantities, the channel was divided into $100 = N_{bins}$ bins, chosen to provide sufficient resolution in narrow channels without generating excessive data in wide channels; the bin width thus depended on channel width. Averaging was typically performed over 10 seconds, once after initialisation, and once in steady state after half the simulation runtime.

Steady state recording

Without noise, only particles that start less than $2 \times R_0$ will hit a channel edge at some point in the simulation. All others will keep circling on the channel surfaces. Even with noise, a significant amount of particles that were spawned in the central region of the channel will keep swimming freely on the channel surface for extended periods of time, i.e. for the entire simulation runtime. For longer simulations, most particles that will eventually reach a wall have already hit it, which we identified as the relaxed system "steady state". Therefore, we stored a system snapshot after half the simulation time, and restarted the statistical evaluation of the simulation as a "second set" of statistics for steady state.

3.2.6 Event recording

Beyond channel geometry, descriptive statistics, and initial conditions, wall attachment and detachment events were also recorded. The algorithm was extended to detect these events throughout each simulation run and store them in a pandas dataframe with the structure shown in table 3.2.

Table 3.2: Attachment and detachment events extracted from consecutive simulation timesteps.

Name	Symbol	Unit	Description
particle_id	i	–	Index of the particle undergoing an event
timestep	t	–	Simulation timestep at which the event occurs
event_type	e	–	Event flag: $e = 1$ attachment, $e = 0$ detachment
x	x_i	μm	x-coordinate of the particle at the collision point
y	y_i	μm	y-coordinate of the particle at the collision point
phi	φ_i	rad	Orientation angle of the particle upon collision
dy	Δy	μm	Difference in y-coordinate at either detachment or after one second
dt	Δt	timesteps	Number of timesteps after which dy is calculated. Usually set at 1000, i.e. 1 s, but can be less if particle detaches before the timer runs out

An attachment (detachment) event is registered whenever the edge-contact flag of a particle changes from 0 to 1 (from 1 to 0) between two consecutive timesteps. The edge-contact flag indicates whether a particle is sufficiently close to the channel wall to be influenced by the wall forces, i.e. when it lies within the ε-region.

Crossing the boundary of this region starts a timer. If a new event—defined as entering or leaving the edge region—is detected, Δy and Δt are calculated and the event is recorded. If no new event occurs, the timer is terminated after 1 s and the event is recorded at that point.

Each record therefore contains the particle index, the timestep, a binary event identifier, the particle position and orientation at the event time, as well as the corresponding Δy and Δt.

These events are subsequently linked to the initial conditions, enabling the analysis of residence times, individual particle histories, and related metrics.

3.2.7 Honorable mention: Data storage and -management

It should be very briefly mentioned that the biggest advance in my data analysis was not an adaptation of simulation or analysis code. In contrast, it was a matter of organizing the billions of data points appropriately. I developed a dedicated workflow to manage simulations and data, which substantially supported the analysis; its details are described in the Appendix. Version and feature control was done in git.

3.3 Terminology and variable definitions for experiments and simulations

As mentioned in the introduction to this chapter, our main goal is to understand the experimentally observed phenomena by comparing the results to simulation data. Due to technical limitations and challenges imposed by real-world conditions, this is not entirely simple. Depending on the definitions can even influence results and conclusions. Therefore I want to explain briefly the concepts of incoming or attachment angle, further denoted by ϑ_{inc}, and their definitions for each experiments and simulations. Furthermore, I will use the terms strong confinement, mild confinement and weak confinement later on to explain some geometric relationships. They will also be defined in this section.

3.3.1 Incoming angle definitions

Experiments

Although the spatial and temporal resolution of the experimental setup is sufficient to reliably capture bacterial trajectories, it is not high enough to resolve the precise shape and orientation of an individual bacterium at a given instant. A geometric proxy for the swimming direction was therefore required.

To this end, an “edge region" was defined in the vicinity of the channel walls, where hydrodynamic attraction to the boundaries is expected to be significant. Within this region, bacterial trajectories typically exhibit pronounced curvature as the cells reorient and align with the walls.

In the experiments, Peixin Zhang implemented a discrete version of this curvature-based definition in order to extract ϑ directly from particle tracks. As before, she first restricted attention to the portions of each trajectory lying within a $5\ \mu$m edge region adjacent to the wall. Within this region, the local curvature was approximated using triples of points on the trajectory, $\vec{p}_1$, $\vec{p}_2$, $\vec{p}_3$, taken at 10-frame intervals (corresponding to a time separation of 1 s between $\vec{p}_1$ and $\vec{p}_3$).

For each such triple, the unique circle passing through $\vec{p}_1$, $\vec{p}_2$, and $\vec{p}_3$ was constructed, and its center was denoted by $\vec{p}_{\mathrm{center}}$. At the middle point $\vec{p}_2$, the tangent to this circle defines the instantaneous swimming direction. This discrete construction is illustrated in Fig. 3.4, which

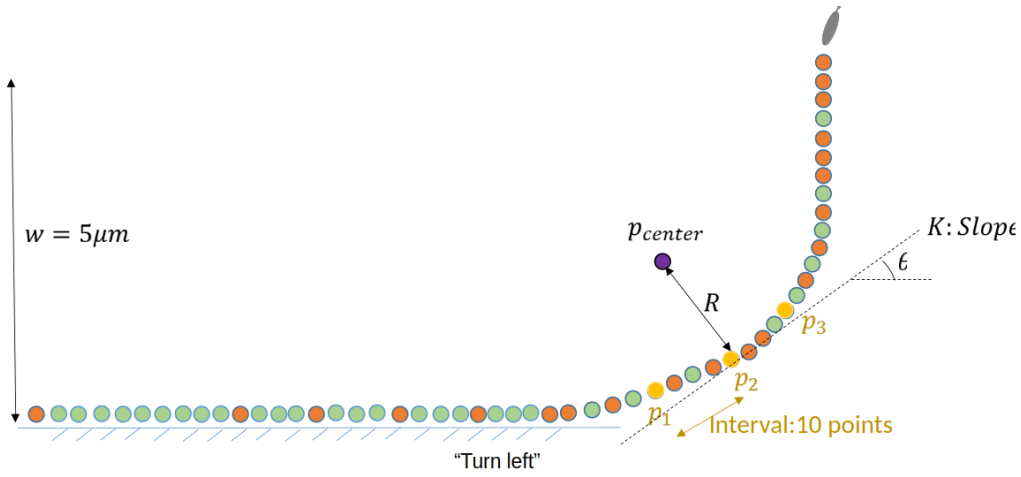

Figure 3.4: Incoming angle definition in the experiments, by Peixin Zhang.

shows the three-point circle, its center, the associated normal and tangent directions, and the definition of the incoming angle with respect to the wall normal.

Simulations

Since in the simulations the instantaneous orientation of a bacterium at timestep i is given by φ_i, defining an angle relative to a channel wall is straightforward. For the definition of the incoming angle ϑ_{inc}, three different cases are considered:

$$\vartheta_{\text{inc}} = \begin{cases} \pi - \varphi, & \text{for the left wall,} \\ -\varphi, & \text{for the right wall if } \varphi < \pi, \\ 2\pi - \varphi, & \text{for the right wall if } \varphi \geq \pi. \end{cases} \tag{3.10}$$

With this definition, the sign of ϑ_{inc} directly indicates the particle orientation relative to the surface normal: a negative value corresponds to a bacterium facing left, while a positive value corresponds to one facing right. This convention is analogous to the definition of ϑ_{inc} derived from experimentally measured particle trajectories described above. The definition is illustrated in Fig. 3.5.

3.3.2 Confinement regimes

To characterize the geometrical conditions of the system, we distinguish between three confinement regimes defined by the relation between the channel width W_0 and the characteristic swimming radius R_0.

Weak confinement corresponds to channels wide enough to allow bacteria to complete circular trajectories without interacting with both walls simultaneously, i.e. $W_0 > 2R_0$.

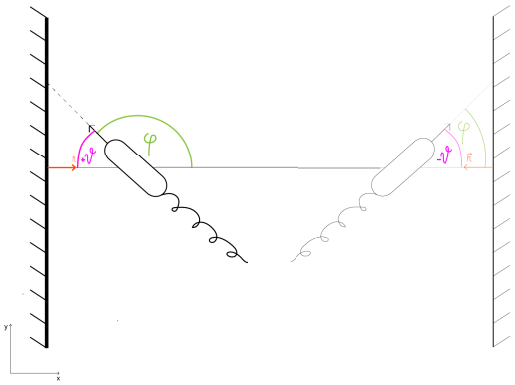

Figure 3.5: Sketch of the definition of ϑ_{inc}. It is defined relative to the particle's perspective and swimming direction; a positive angle always denotes an approach "right" from the surface normal, a negative one "left".

In the regime of mild confinement, the channel width restricts full circular motion but still allows bacteria to perform partial arcs and reorient within the channel. This regime is defined by $R_0 < W_0 < 2R_0$.

Finally, strong confinement describes channels narrower than the swimming radius, $W_0 < R_0$. In this case, particles quickly reattach to the channel walls and have limited freedom to reorient, apart from diffusive motion near the boundaries.

4 Results & Discussion

4.1 Free particle trajectories and wall attachment

As expected, the particle trajectories recorded in the experiments closely resemble those obtained in the simulations. A snapshot of experimentally recorded trajectories in two-dimensional Eulerian coordinates is shown in Fig. 4.1.

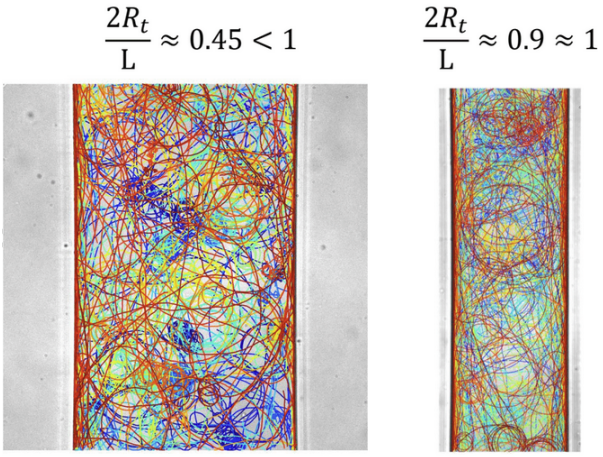

Figure 4.1: Experimental particle trajectories recorded by Peixin Zhang in two dimensions, viewed from the bottom of the channel. A clear accumulation of particles near the walls is visible, while trajectories on the free surface exhibit a wide range of swimming radii. Note that here the channel width is denoted with L.

The simulated trajectories show a very similar overall structure, although they appear more homogeneous due to the controlled simulation parameters. An example of simulated particle trajectories in a channel is shown in Fig. 4.2.

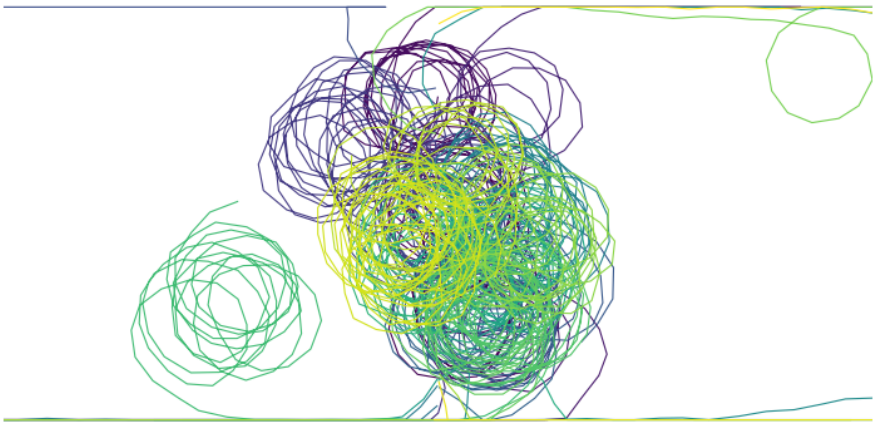

Figure 4.2: Typical simulated trajectories in a $40\ \mu$m wide channel. For each simulation run, the swimming radius is kept constant. Here, it is set to $R_0 = 10\ \mu m$.

Consistent with observations reported in numerous experimental studies over the past decades, bacteria observed from below a channel surface move predominantly in clockwise circular trajectories on the free surface.

Individual trajectories, however, still exhibit small variations in curvature and occasional changes in direction due to stochastic effects. A few representative examples from experiments by Peixin Zhang are shown in figure 4.3.

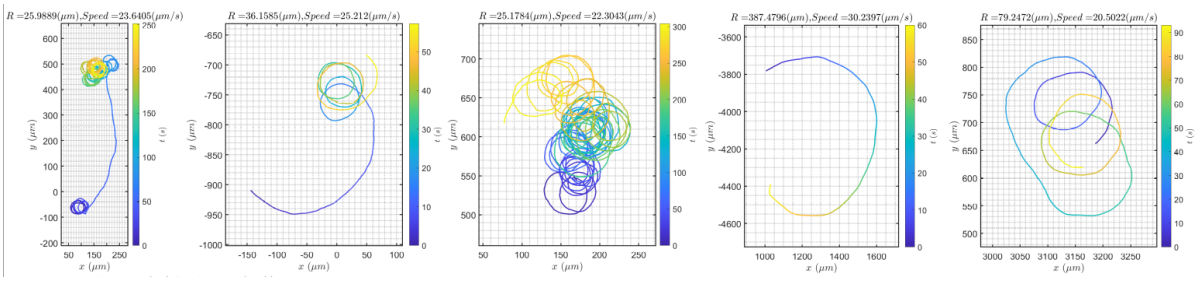

Figure 4.3: A few selected particle trajectories with their calculated global swimming radius and measured speed. Recorded and plotted by Peixin Zhang.

4.1.1 Experimental trajectory curvature analysis

As can already be seen by comparing Fig. 4.1 and Fig. 4.2, particle initialization and swimming radius can be controlled much more precisely in the simulations than in the experiments. To improve the comparison between simulations and experimental observations, our collaborators attempted to estimate a distribution of swimming radii from the experimentally recorded trajectories. One advantage of the simulation framework is that it can incorporate a distribution of swimming radii rather than a single fixed value.

Figure 4.4 illustrates typical experimentally measured bacterial trajectories. When viewed from the bottom of the channel, the trajectories exhibit a clear clockwise (CW) curvature.

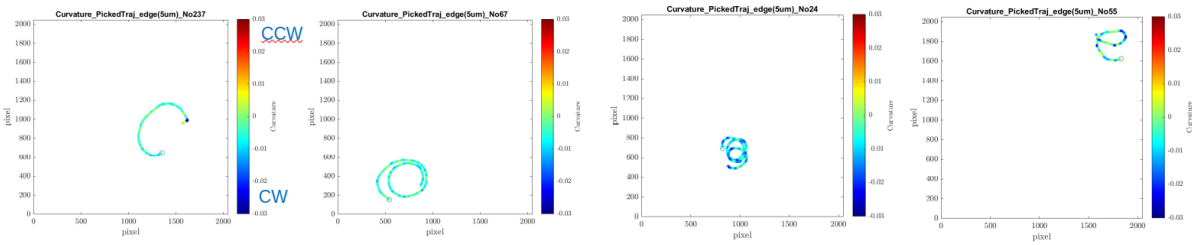

Figure 4.4: Example experimental trajectories showing the clockwise curvature of bacterial motion when observed from the bottom of the channel.

From these experimental trajectories, a distribution of swimming radii was extracted, as shown in Fig. 4.5. The swimming radius, or “global curvature," was defined as follows. Because the local curvature along the trajectory is strongly affected by noise, a global measure was constructed by averaging the curvature along the entire trajectory. The direction of rotation was then determined from the sign of this mean curvature.

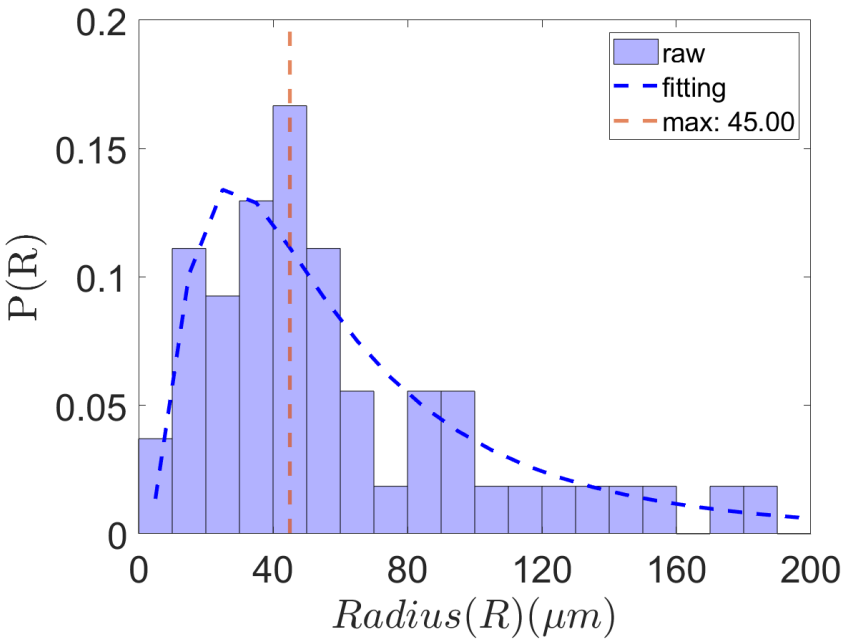

Figure 4.5: Normalized histogram of global swimming radius, derived from experimental measurements. By Peixin Zhang

4.2 Probability density

In section 2.2, we saw that active brownian spheres accumulate at channel walls and edges. In the simulation steady state, almost all particles gather at channel edges. Without noise, some would never reach the walls; with noise, bacteria starting farther away take longer because they

rely on diffusion. Thus, in wide channels a "bulk" forms in the middle where bacteria move without hitting the walls, as shown in figure 4.6 for selected simulation runs.

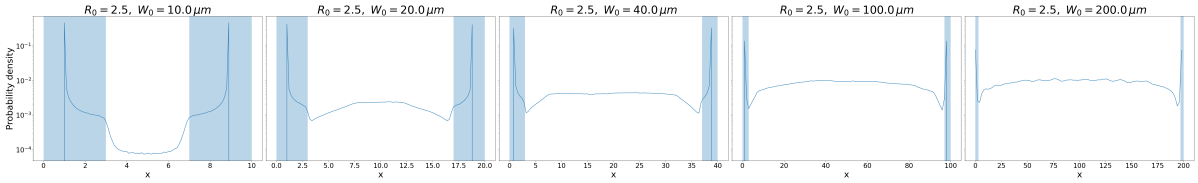

Figure 4.6: Probability density of particle positions within the channel for a selected subset of simulation trajectories. The ordinate is displayed on a logarithmic scale to enhance the visibility of the wall-interaction region, indicated in blue.

Figure 4.6 shows the strong influence of the wall interaction region on the particle position statistics. The wall interaction region has a fixed size of $\varepsilon = 3\ \mu m$. Naturally, it occupies a larger fraction of the channel at smaller channel widths. This, in turn, results in a larger fraction of bacteria being affected by the presence of channel walls. Another key observation is the steady-state particle concentration near the channel edges, which depends on channel geometry. Without noise, a particle that starts farther from the nearest wall than its swimming diameter will never reach a wall. With noise, diffusive effects give a small probability that particles eventually reach the wall, as illustrated in figure 4.7.

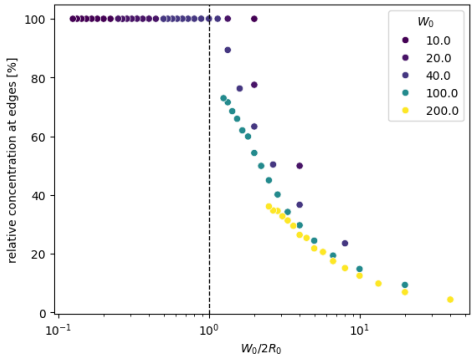

(a) Perfect circle swimmers without diffusion.

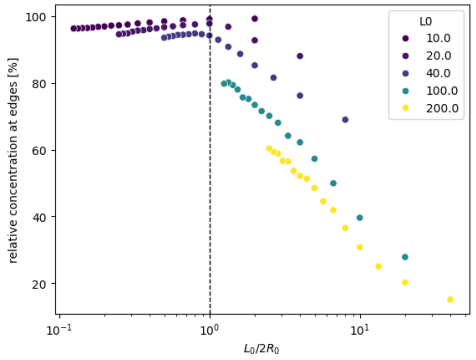

(b) Particles under the influence of physical diffusion coefficients.

Figure 4.7: Relative concentrations in edge bins as a function of channel width and swimming diameter $2R_0$

In steady state without noise, all particles that can reach the wall do so and then never detach; detachment is only possible through diffusion. For very small channels, where $\varepsilon >> W_0/N_{bins}$, the edge bins (the outermost x-bins) do not cover the entire wall interaction region, which explains why the data points for the smallest channel widths in figure 4.7b deviate from 100% edge concentration. Without noise, particles attached to the wall also never leave; this process is purely diffusive. In both subplots, the curvature of the declining branch of the edge-bin concentration results from the uniform distribution of particle orientations within the initialization bin.

Particles starting parallel to the wall, oriented along $\hat{e}_y$, may never reach the edge even if they are initialized close to the boundaries. This effect will be discussed further in later chapters on geometric considerations. These results agree reasonably well with the experiments, although the experimentally occupied edge regions are wider and the role of Brownian noise is more significant. As shown in figure 4.8, the experimental resolution is lower due to the 5 μm bin width. This coarser binning can be advantageous when only limited data are available. As indicated in the plot, the number of experimental tracks, $N_{tracks} = 149$, is several orders of magnitude smaller than the 10^5 simulated trajectories. The data are normalized by the channel width L.

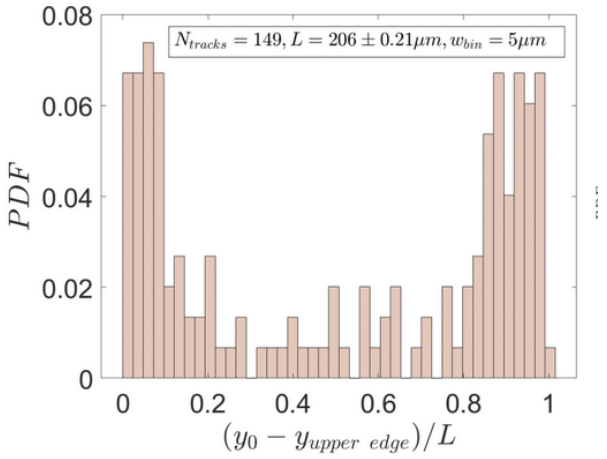

Figure 4.8: Probability density function PDF from experimental data by Peixin Zhang. Note that here the channel width is denoted by L.

The edge concentration analysis yields similar outcomes for experimental data and simulated trajectories. These results also agree with earlier work, from the first measurements of confined microswimmer distributions to recent simulations and experiments [14, 41, 51].

4.3 Particle velocities and edge orientation

This is where it becomes interesting. As explained in the introduction, under certain circumstances *E. coli* were observed to swim along channel edges not in the direction of their circular trajectories, but in the opposite direction. We reproduced this effect with the simple wall interaction procedure, but found it to be highly dependent on channel geometry. Analogous to the particle position probability density across the channel width, we plotted the average velocity $\bar{v_y}$ for each channel bin and each combination of W_0 and R_0. Figure 6.2 shows the velocities for one swimming radius and various channel widths. Regions with net motion in negative y-direction are red; those with positive motion are blue.

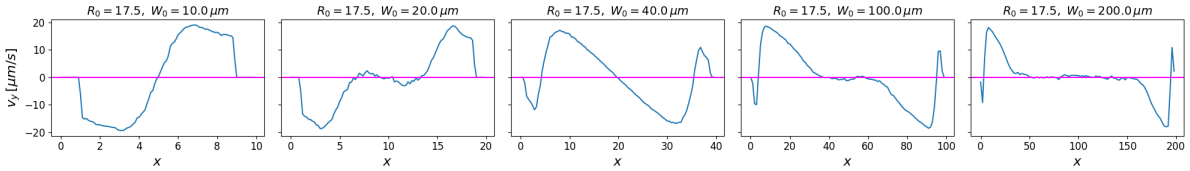

Figure 4.9: Average speed parallel to the walls, v_y, across the channel width for $R_0 = 17.5\mu m$. For small channel widths, bacteria reverse their preferred swimming direction. For $W_0 \gg 2R_0$, they behave according to naive expectations. The "counterpeaks" in the channel center are marked in green.

Figure 6.2 shows that our method reproduces the inversion of swimming direction in narrow channels. One would naively expect bacteria to swim up along the left wall and down along the right, which is true only for wide channels. For certain geometries, we also observe velocity "counterpeaks" on both side of the channel, arising from bacteria circling in the channel center. Near $W_0 = 2R_0$, most particles attach to the walls; only a few can still complete a circle within the channel. This effect is illustrated in the sketch 4.10 below.

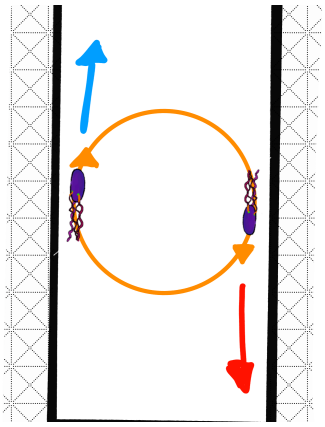

Figure 4.10: Sketch to illustrate the influence of free circling bacteria in the middle of the channels, the cause of the velocity "counterpeaks" at channel geometries close to $W_0/2R_0$. All other particles attach to the closest wall after initialization. For wider channels, more bacteria can circle freely, and the velocities cancel eachother out statistically.

However, in the edge interaction regions of the channel, the preferred moving direction is *always* to the left. To illustrate this, as it will become important later on, we have "zoomed in" on the region from the left edge to 5 μm distance in figure 4.11. We we can see that the resolution gets worse and the peaks become less pronounced. This is due to the fixed bin count, which at wider channels result in larger bins. Therefore, also regions outside of ε are included in the averaging.

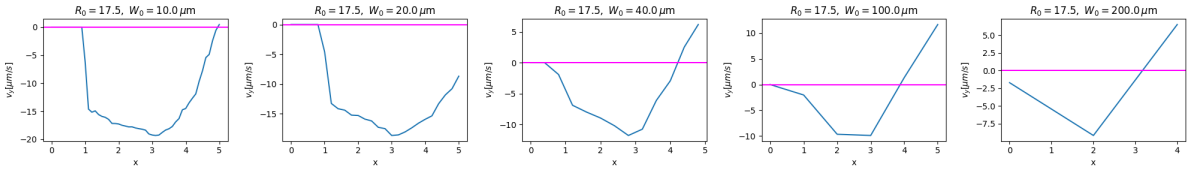

Figure 4.11: "Zoom" of the v_y - plots for the left channel edge and a region of 5 μm.

The particle flux in a given direction is difficult to measure experimentally due to limited statistics. Therefore, the experimental data were first analyzed in terms of *orientation*, i.e., swimming direction near the edges. These results show the same effect: swimming direction is reversed in narrow channels, as in figure 4.12.

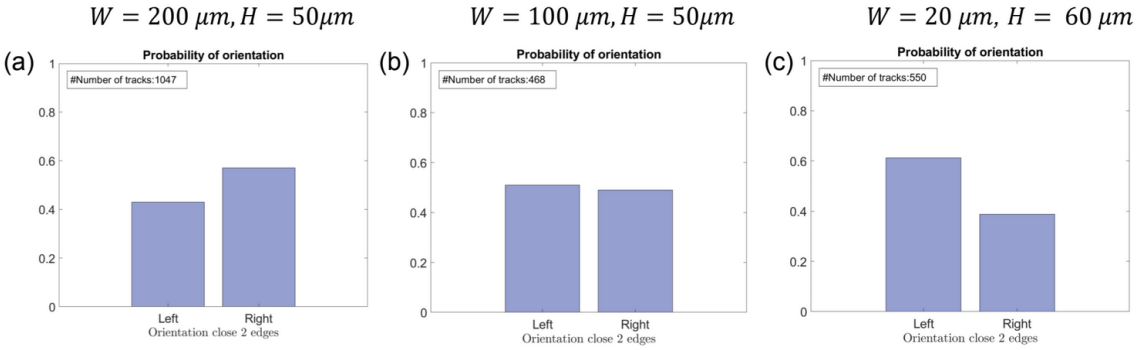

Figure 4.12: Orientation of swimming bacteria close to the channel walls, derived from experimentally observed particle trajectories by Peixin Zhang.

4.3.1 Steady state maps

Most statistics show similar qualities in the experiments and simulations. However, it is unclear whether this reflects accurate model reproduction or coincidence. We plotted their orientations as a function of their positions in the channel and found interesting trends.

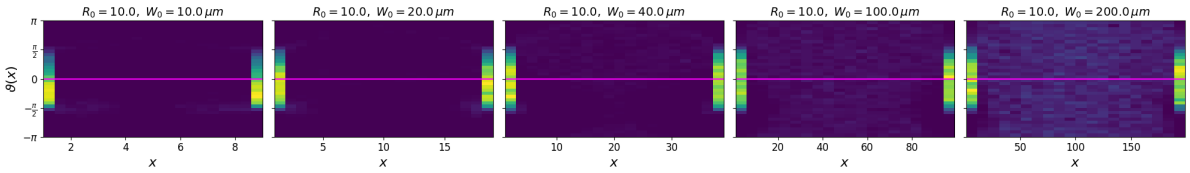

Figure 4.13: Orientation ϑ of particles close to the wall in simulation steady state for R_0 = 10 μm.

As shown in 4.13, particles in the simulations tend to align approximately perpendicular to the confining wall. Equivalently, particles that orient parallel to, or pointing away from, the wall are more likely to diffuse away from the boundary and leave the near-wall region more rapidly. Notably, for small confinement geometries there is a slight bias toward negative orientation

angles, indicating that particles are more likely to point opposite to their intrinsic preferred swimming direction. This bias reverses under weak confinement.

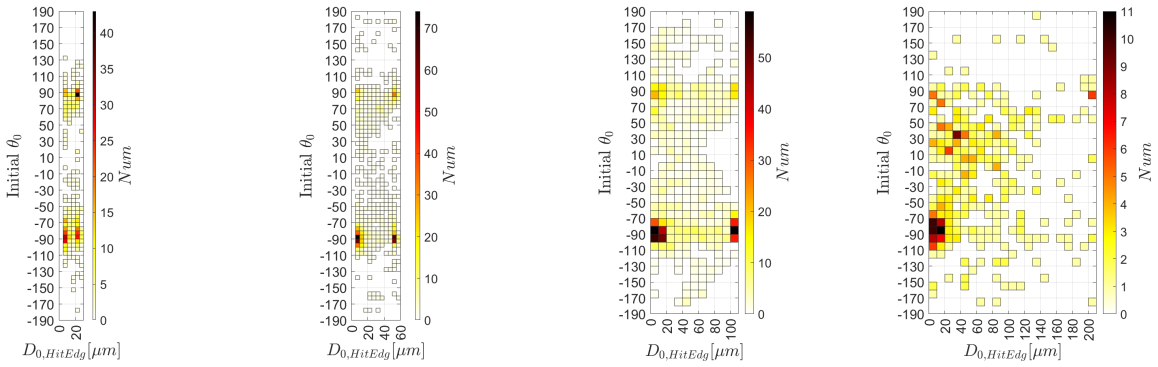

(a) $W_0 = 20\,\mu\mathrm{m}$ **(b)** $W_0 = 50\,\mu\mathrm{m}$ **(c)** $W_0 = 100\,\mu\mathrm{m}$ **(d)** $W_0 = 200\,\mu\mathrm{m}$

Figure 4.14: Maps of number of particles in bins over distance from the edge a bacterium is going to hit, as well as its initial theta in relation to that edge for four different W_0.

The comparison with experimental probability maps for orientation and distance bins shows a clear bias for particles near the edges to align parallel to the wall. Under strong confinement, we observe both orientations, contrary to our initial expectations, although experimental limitations (like limited data availibility) may contribute to this. Nonetheless, the results are consistent with theory and previous observations that bacteria align parallel to walls.

4.4 Particle fluxes

Superimposing particle concentration at the walls and y-velocity v_y shows that the "counterpeaks" in figure 6.2 are negligible, as nearly all particles accumulate at the wall edges and thus solely determine the net particle fluxes. The same figure also indicates that channel width governs both particle swimming direction and edge flux orientation, consistent with Peixin Zhang's experimental results in figure 4.15.

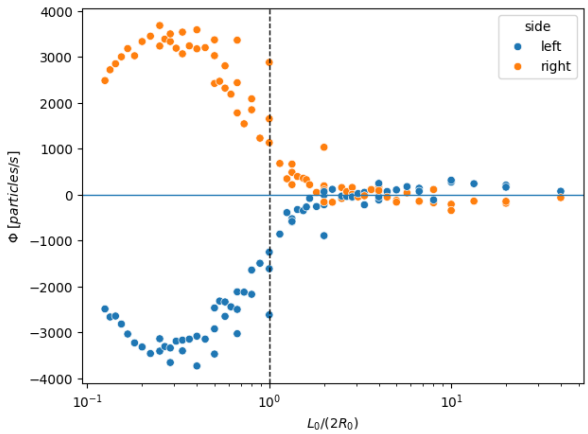

Figure 4.15: The total particle flux through the left and right halves of the channel is plotted versus the dimensionless ratio $W_0/(2R_0)$ for steady-state simulations. Fluxes are obtained by integrating binned local fluxes on each side of the channel midpoint. The dashed vertical line at $W_0/(2R_0)$ marks the transition between weak and strong confinement. As confinement increases, the asymmetry between left and right fluxes grows. Only data measured in steady state is considered.

The figure shows the total particle flux through the left and right halves of the channel versus the dimensionless geometric ratio $W_0/(2R_0)$.

For each simulation, the local particle flux is obtained from binned trajectory data and integrated over the left and right halves of the system, defined relative to the channel midpoint $x = W_0/2$. Fluxes are calculated in particles per second and, when enabled, normalized by the total particle number to allow comparison between runs with different particle counts.

The data is plotted on a logarithmic horizontal axis to highlight variations across a wide range of confinement ratios. The vertical dashed line at $W_0/(2R_0) = 1$ marks the transition from weak to mild geometric confinement. It is immediately visible that net directional transport systematically depends on $W_0/(2R_0)$. In mildly confined cases, left and right fluxes become similar.

4.5 The role of symmetries

Channel geometry is the main factor determining *E. coli* orientation near walls under confinement, in both simulations and in vitro. However, because the simulations are fully symmetric, they yield no net flux; some mechanism must break this symmetry. Our next goal was to determine how the bacteria "choose" their swimming direction and to uncover the mechanisms behind the different orientation preferences under strong confinement.

4.6 Incoming angle and wall swimming direction

We now know that most bacterial flux occurs along the edges of our rectangular channels. Once bacteria attach to an edge, they tend to stay there and largely keep their orientation. Our next question is what happens *before* attachment to the channel wall. A key quantity is the angle at which a particle collides with the wall. Because the mechanics are symmetric on both sides of the channel, we define an *incoming attachment angle* ϑ_{inc} as the angle between the particle's unit direction vector as it approaches the wall and the normal vector of the channel edge, $\bar{n}_{wall}$, as explained in the methods section.

4.6.1 Incoming angle vs. swimming direction

We next examined the relationship between incoming angle and swimming direction. The experimental data clearly showed a direct correlation, as plotted in figure 4.16.

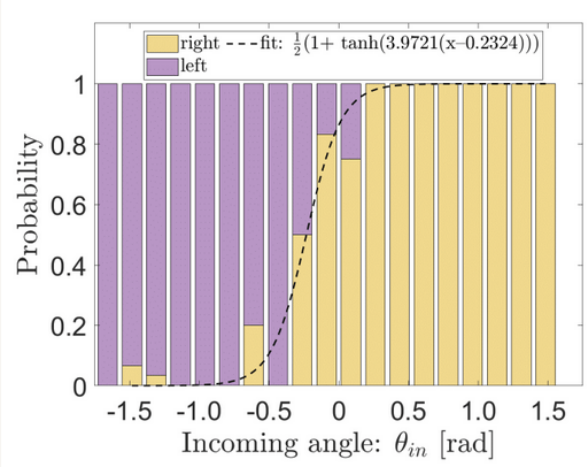

Figure 4.16: Incoming angle relationship to swimming direction. Data derived from experimental observations by Peixin Zhang

Almost all particles arriving with an incidence angle to the left of the channel normal swim left; the same holds symmetrically for the right. If we draw the 50% probability line, the tanh curve is slightly shifted to the left. This likely results from how the incoming angle $\vartheta_{incoming}$ is defined: it is measured far enough from the edge that the bacterium can begin turning toward its preferred swimming direction. Repeating the analysis with simulation data shows that this relationship is almost independent of channel width and swimming radius, as it has the same form for all combinations of W_0 and R_0. The arrival angle at which a swimmer enters the wall interaction region solely determines how it attaches and in which direction it swims afterward, as seen in figure 4.17.

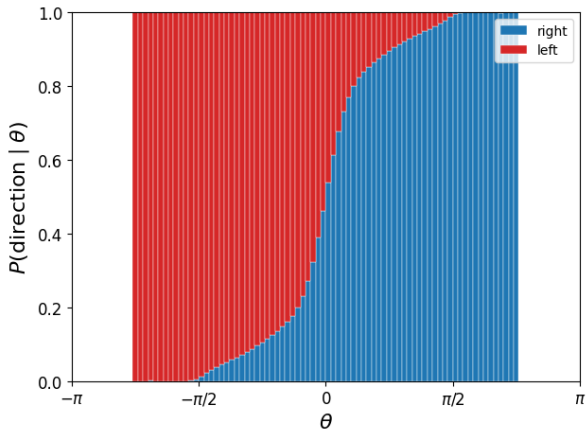

Figure 4.17: The same relation as in figure 4.16, derived from simulated trajectories under the influence of noise, considering all incoming attachment events over all simulation runs. Movement direction is measured within 1 s after attachment, or before the particle detaches again.

An important factor is the slope of the fitting curve. In the plot from data simulated without diffusion, we obtained only two uniformly colored bars: particles with a positive incoming angle always swam to the right after attachment, and those with a negative angle always swam to the left. Particles arriving exactly normal to the wall did not move but remained at their attachment site. Note that the orientations $-\pi$ and π are identical, so in this case noise determines the swimming direction.

Another key difference between the two plots is the steepness and shape of the relationship. The experimental plot follows a hyperbolic tangent, likely linked to hydrodynamic forces near the edge. Diffusion matters only until bacteria are close enough for the hydrodynamic alignment described in the introduction. These forces both attract particles to the wall and rapidly align them parallel to it. We will see this again when examining particle angles relative to the nearest wall during steady-state swimming later on. In contrast, the simulation data shows a very clear and symmetric relationship between the incoming angle and the movement direction of a particle within the first 1 s.

4.7 Initial conditions

Now that we know the incoming angle is the only factor determining the movement direction after attachment, we ask what happens before attachment. We consider all factors in a bacterium's history that could influence how it arrives at a wall.

In simulations, this is straightforward to control. As explained in the Methods, the algorithm can take a histogram of initialization parameters as input and initialize N particles in every φ and x bin. To relate initial conditions to attachment accurately, we use 10° steps for φ and 20 equidistant bins for x. We first checked the probability that a particle initialized with given φ and x in the channel would go "left," i.e. arrive with $\vartheta_{inc} < 0$. I selected simulations with R_0 = 5 μm, shown in figure 4.18:

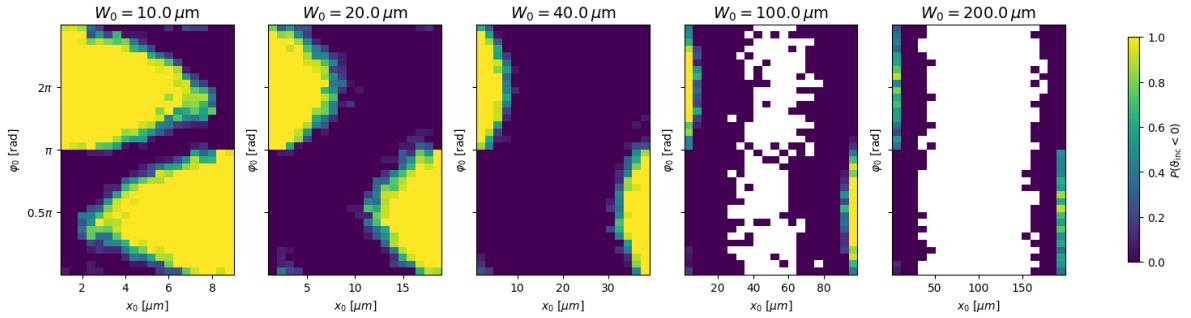

Figure 4.18: Probability that a particle starting at φ_0 and x_0 reaches the wall with incidence angle $\vartheta_{inc} < 0$. Dataset from simulations with swimming radius $R_0 = 5$. White points indicate missing data, where particles did not reach the wall during the run time.

The figure shows that the incoming angle is strongly correlated with the particle's starting point and initial orientation, following an almost sinusoidal pattern. Once the setup enters the "weakly confined" regime, i.e. $W_0 > 2R_0$, some particles never reach a wall and instead circle freely along the channel surface.

Because this result is still symmetric, we changed our analysis from absolute x–y coordinates to a description relative to the wall the particle eventually hits. We record the initial conditions at $t = 0$ and link them to particle IDs in the attachment database. For each ID, we then collect all events and qualitatively reconstruct the particle's trajectory.

In figure 4.19, for each particle we identify the first wall it hits, the impact angle, and the initial distance to that wall. Note that ϑ_0 is not the impact angle but the initial angle between the particle orientation and the wall normal, extrapolated to the particle center.

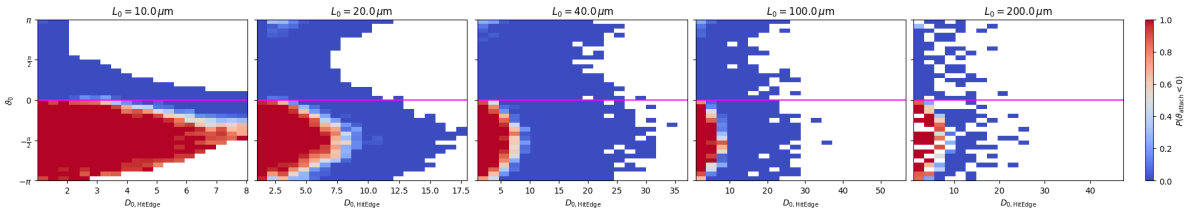

Figure 4.19: Probability of a particle colliding with a channel edge with $\vartheta_{attach} < 0$ as a function of its initial distance to said edge. Data from simulations with swimming radius $R_0 = 5\ \mu m$.

Let us now take a closer look at this figure. Although the pattern remains symmetric overall, it shows more clearly that particles are *more likely* to attach while oriented to the left and consequently to swim leftward. Under strong confinement, the red regions dominate and occupy a larger fraction of phase space than the regions corresponding to motion to the right. These plots already suggest that the grainy regions are caused by noise, whereas the effect itself is purely geometric. To demonstrate this, we generated the plot in figure 4.20 from trajectories simulated without diffusion.

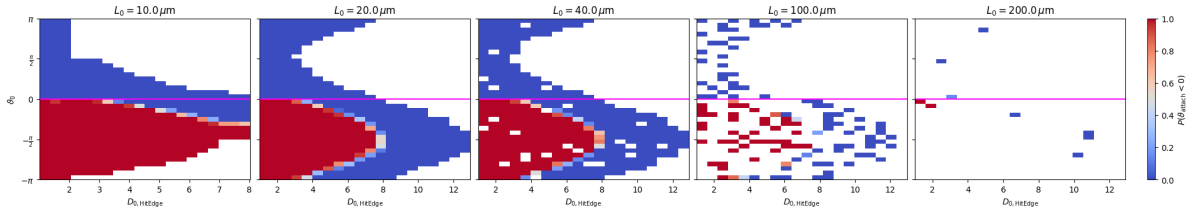

Figure 4.20: Reconstruction of figure 4.19 from simulation data without noise. All other parameters were kept unchanged.

The curve shapes remain unchanged, but the sharp boundary at which particles switch from hitting the left-facing edge to hitting the right-facing edge becomes much clearer. How do these plots compare with the experiments, and to what extent can their conclusions be transferred to experimental conditions? Figure 4.21 shows attachment preferences similar to those observed experimentally, including the same sinusoidal character.

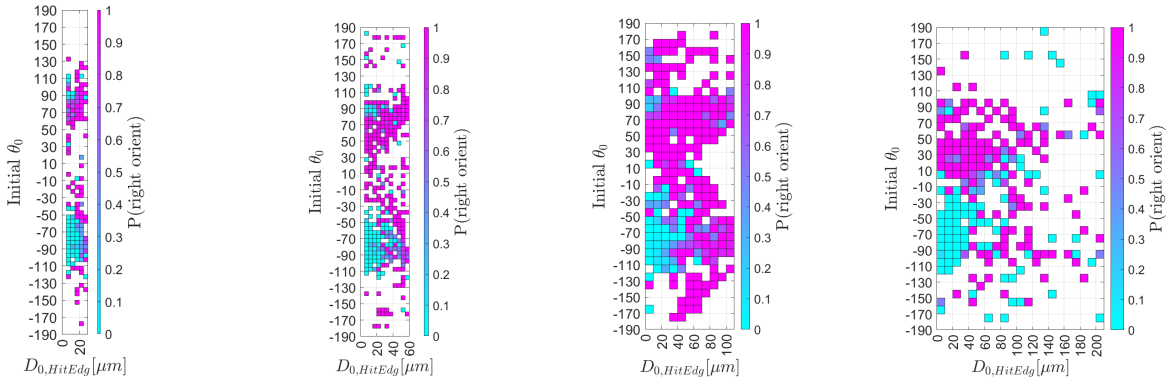

(a) $W_0 = 10\,\mu\mathrm{m}$ **(b)** $W_0 = 20\,\mu\mathrm{m}$ **(c)** $W_0 = 100\,\mu\mathrm{m}$ **(d)** $W_0 = 200\,\mu\mathrm{m}$

Figure 4.21: Probability maps of the initial attachment angle as a function of the initial distance to the next edge for different channel widths W_0.

In the experimental data analysis, data density and availability are lower, but the tendencies and patterns are similar: the shape of the "go left" patch in the bottom left has the same sinusoidal quality as in the simulations. This shows that the initial conditions determine the angle at which particles hit the edges and thus correlate directly with their swimming direction in the channels. It is important to note that "initial conditions" in experiments are an arbitrary description of the system state: there is no true initial state because the bacteria always have a history, and we only observe a snapshot in time. We will return to this in the conclusions.

4.8 Geometric considerations

4.8.1 Particle starting point and orientation vs. wall hitting angle

The angle at which a particle at distance D_0 from a singular wall hits that wall is mainly set by its initial orientation. Figures 4.18 and 4.19 show this only for a subset of simulations at fixed swimming radius R_0.

We now analyze this more generally. Consider ideal circle swimmers, unaffected by diffusion, near a singular wall at $x = 0$ (left) and unconstrained to the right. Take a particle with initial orientation $\vartheta_0 = -\pi/2$, parallel to the wall and facing left. If it starts close enough to feel hydrodynamic interactions, it will swim toward the wall. As we move it away, it will still hit the wall at a negative angle until its distance exceeds the swimming radius R_0. At $D_0 = R_0$, the particle has moved a distance R_0 along $-\hat{e}_y$ and rotated by $\pi/2$, so $\vartheta_{\text{inc}} = \vartheta_0 + \pi/2$. For $\vartheta_0 = -\pi/2$, it then arrives exactly normal to the wall. If we move it even farther, the sign of ϑ_{inc} becomes positive: the particle hits the wall with $\vartheta_{\text{inc}} > 0$ and then swims along the wall in the direction opposite to its initial one. This remains true until the starting distance exceeds $2R_0$ (the swimming diameter); beyond that, without noise, the particle can no longer reach the wall.

The key point is that D_0 and R_0 only matter through their ratio; any pair (D_0, R_0) with the same ratio yields the same qualitative behavior.

Conversely, fixing $D_0 = R_0$ and varying the initial orientation, we obtain the same structure. At $\vartheta_0 = \pm\pi$, the particle just reaches the wall in its preferred circling direction after traversing $3/4$ of a circle; at $\vartheta_0 = -\pi/2$ it arrives normal to the wall, and for $\vartheta_0 > 0$ it no longer reaches the wall and circles freely.

These combined effects are illustrated in 4.22.

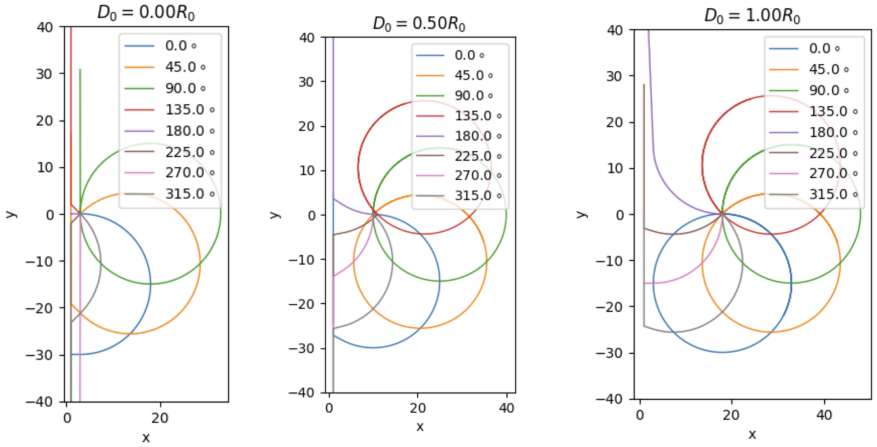

Figure 4.22: Particles of various orientations starting at distances of different multiples of their swimming radius.

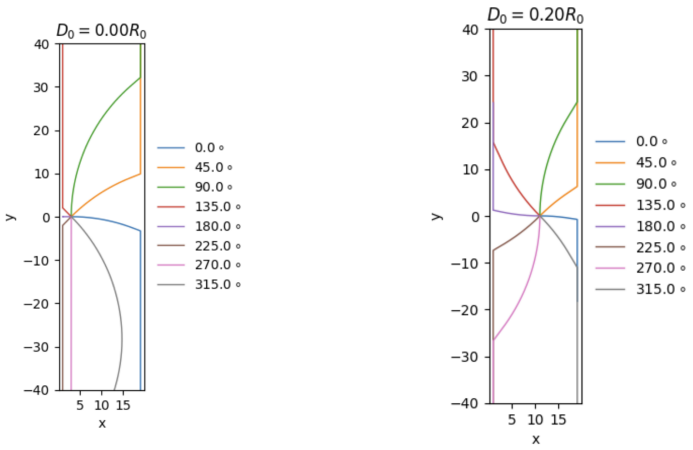

Figure 4.23: Possible incoming particle angles depending on their position in the channel and their initial orientation.

4.8.2 Total setup geometry

The last chapter shows that the initial configuration relative to the channel walls determines a particle's edge-swimming direction. However, a single particle's direction does not characterize the edge fluxes. Instead, we must describe the total probability for particles to arrive at a given angle as a function of channel geometry.

Note that in figure 4.22, not all initial configurations are possible when the channel width is $W_0 < 2R_0$. Under such strong confinement, one wall is always closer than the trajectory diameter, so particles always have two possible wall-collision options, but one is necessarily nearer. From the previous section, we know that the closer a particle starts to a wall, the more likely it is to swim to the right for a random initial orientation. Because one wall is always very close in narrow channels, the probability that particles "swim left" grows as the channel width decreases. This behavior is illustrated qualitatively in figure 4.23.

We can also view this by taking a random particle with a random initial position and orientation in the channel and then "moving the walls closer," as sketched in figure 4.24 below.

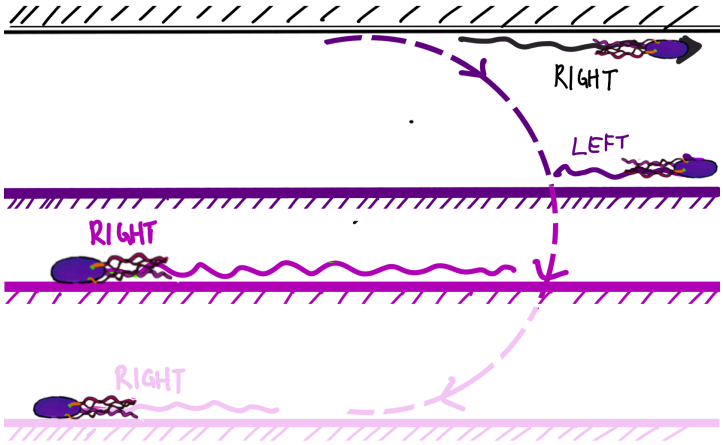

Figure 4.24: Sketch illustrating the effect of a smaller channel geometry and stronger confinement on possible attachment and swimming directions.

Looking back at the plots of initial distance to the walls and orientation in 4.19, expressed as D_0/R_0, they should all look similar. This is because, under mild and strong confinement, particles have two possible attachment points to the walls, which changes the probability distribution throughout the channel. The qualitative differences are shown in figure 4.25.

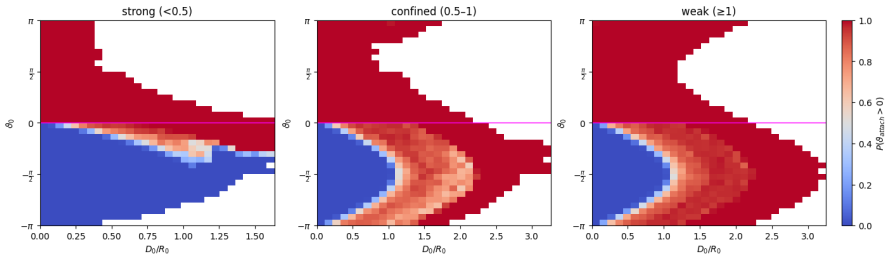

Figure 4.25: Attachment angle dependant on particle starting point, showing the qualitative differences for the three confined spaces.

4.8.3 Analytical description of channel and trajectory geometries

Francisco Goio Castro, also from ESPCI Paris, conducted a mathematical analysis of the three confinement cases defined in chapter 3. In the following, initial particle distribution of random and uniform form in space and orientation

$$P(x, \vartheta_0) = \frac{1}{2\pi W_0} \tag{4.1}$$

are considered. The total probability for any randomly initiated particle to "go right" is calculated in each step.

Weakly confined particles at $2R_0 < W_0$

As we could also see in the simulation case, for weak confinement, not all particles will even hit a wall. The probability of a particle of random orientation and initial position on the x-axis within the channel (without noise) ever hitting a wall is given by

$$P_{Hit} = \frac{2R_0}{W_0} \tag{4.2}$$

Then, we can calculate the probability to hit the left or the right wall, respectively, at an angle right of the wall normal in the equation below.

$$P(+, Hit) = \frac{1}{\pi W_0}\left(\int_{-\pi/2}^{\pi/2} d\vartheta_0 R_0 + \int_{\pi/2}^{3\pi/2} d\vartheta_0 R_0(1+\cos\vartheta_0\right) = \frac{2R_0}{W_0}\left(1-\frac{1}{\pi}\right) \tag{4.3}$$

The total probability for a particle to go right in case it *does* hit the wall is

$$P_{right} = \frac{P(+, Hit)}{P(Hit)} = 1 - \frac{1}{\pi} \tag{4.4}$$

Mildly confined case: $0.5W_0 < R_0 < W_0$

Here, all particles will hit a wall, and the total probability for a particle to "go right" depending on channel geometry is

$$P_{right} = 1 - \frac{2R_0}{\pi W_0} \tag{4.5}$$

Strong confinement: $R_0 > W_0$

This case is the most complicated. Francisco Goio Castro derived equation 4.8.3 for this case in the following form. For improved readability, the subscripts of W_0 and R_0 are omitted here.

$$P_{\text{right}} = \frac{W\arccos\left(-\frac{W}{R}\right) - W\arccos\left(\frac{-W+R}{R}\right) + R\sqrt{\frac{-W^2+R^2}{R^2}} - R\sqrt{\frac{W(-W+2R)}{R^2}} + R\arccos\left(\frac{-W+R}{R}\right) - R}{2\pi W}$$

Conclusions and rescaling with experimental data

The total probability for particles to attach left or right on either wall is represented in figure 4.26 below.

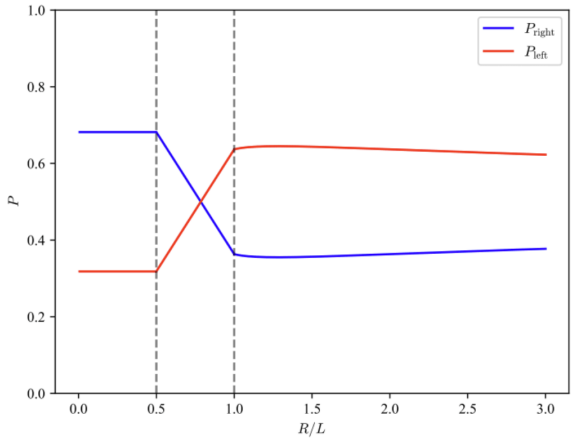

Figure 4.26: Analytical probabilites for particles to go left or right, depending on setup geometry. Here, L is denoting the channel width, otherwise denoted as W_0, and R is the particle swimming Radius. Credits to Francisco Goio Castro.

It is the main conclusion of this thesis that the simulation and experimental results closely resemble this prediction, indicating that geometry is the primary factor determining the orientation preference of *E. coli* under confinement. The corresponding experimental and simulation plots are shown in figures 4.27 and 4.28.

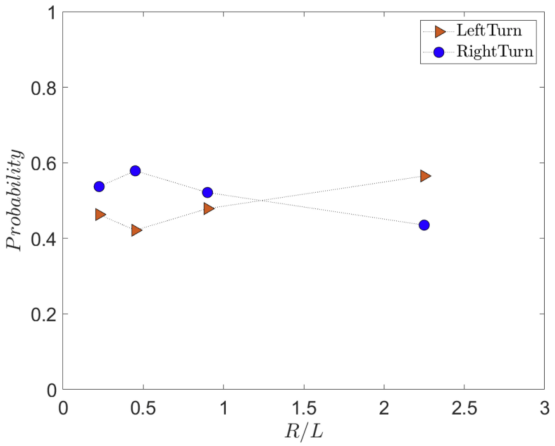

Figure 4.27: Reproduction of figure 4.26 from experiment data. Since channel production is difficult, datasets are limited. Qualitatively, however, they are similar. By Peixin Zhang

Figure 4.28, constructed from simulation data, shows an even stronger bias for the strongest confinement cases. This arises from the "wall interaction region," which affects particles as soon as they spawn there. The mechanism is, of course, more intricate for real-world trajectories.

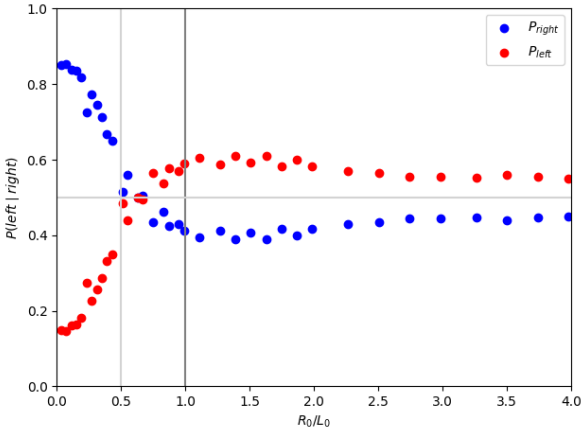

Figure 4.28: The same probability description depending on setup geometry, showing similar qualities to the plots above. Note that here, only attachment events that detach at some point in the simulation are counted. For small confinements, a lot of particles never detach, which could explain the discrepancy in the lower ratio regions. However, this data remains to be analyzed and understood further.

Simulating the probability that bacteria "go right" as a function of trajectory radius for three different confinements yields the relationship shown in figure 4.29.

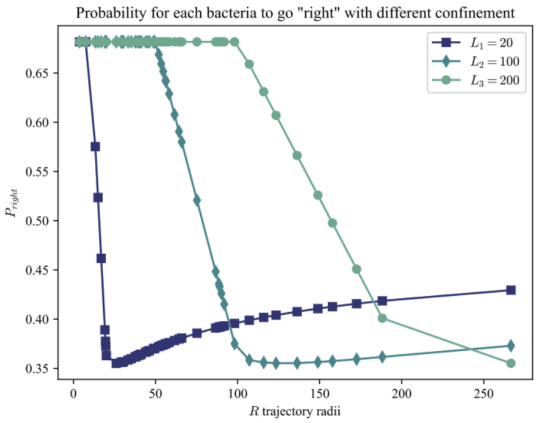

Figure 4.29: Analytical probabilities for particles to "go right" dependant on their confinement and trajectory radius. By Francisco Goio Castro

Figure 4.29 shows a "sweet spot" for left attachment at a width–to–swimming-radius ratio of about 1 for all channels. This indicates that this ratio governs particle attachment preference.

In practice, channel widths are usually fixed, so it is natural to rescale this curve using the empirically observed distribution of particle swimming radii. The resulting plot, 4.30, confirms the expectation: once we move from strong to weak confinement, right attachment—along the preferred swimming direction—dominates.

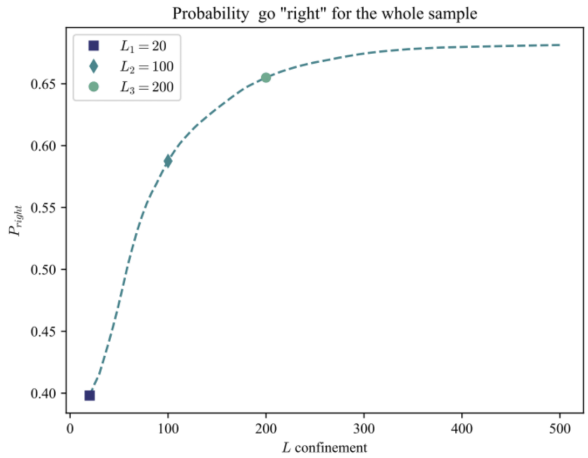

Figure 4.30: Probabilities of attachment to the right side of the wall normal, rescaled using the experimental particle radius distribution and calculated for the three confinements tested. By Francisco Goio Castro

4.9 De- and reattachment analysis

In this section, we have analyzed what determines attachment to walls and how bacteria swim along them. But what happens later, once all particles have had time to reattach and a "steady state" is reached? To answer this, we again group attachment, detachment, and reattachment events. Thanks to how these events were recorded in the simulations, the analysis is straightforward. We distinguish eight cases, described in the following sections.

4.9.1 Reattachment on same wall side

Left to left - LL

Consider a particle swimming to the left in a narrow channel, oriented *against* its usual swimming radius. Due to a tumbling event or random noisy reorientation, it can detach from the wall. Once it is far enough away to be free from hydrodynamic wall interactions, it starts circling again and immediately turns back to the wall, as shown in figure 4.31a. Since this occurs as soon as the particle leaves the "wall interaction region," we expect this type of event in any channel geometry.

Left to right - LR

Our particle again travels left and detaches. Under what conditions could it reorient and reattach on the same side but in the opposite direction? In our setup this is very unlikely. In reality, it could occur either through a series of interactions with the surrounding medium that gradually reorient the bacterium, or via a tumbling event that nearly reverses its direction. Under very strong confinement, the bacterium feels the walls almost everywhere in the channel, so circling motion becomes less important. Detachment and reattachment are then dominated by Brownian motion and random reorientations. This makes such an event comparatively more likely under strong confinement than other de-/reattachment events, simply because all events are more diffusion-driven. I did not find a trajectory that clearly shows this process, but it seems physically reasonable.

Right to left - RL

The case is similar for right-to-left events. If a particle swims right, it is already aligned with its preferred direction. When it leaves the wall due to rotational diffusion, it will likely resume circling near the wall with an orientation $\pi/2 \leq \vartheta \leq \pi$. As shown in before, if we treat this as its starting position, it would, in principle, complete a full circle without hitting the wall again, provided the channel is wide enough. If the channel is too narrow, it will attach to the opposite wall. The only exception occurs if random diffusion effects combine in a very unlikely way.

Right to right - RR

If the channel is wider than the swimming diameter, $W_0 \geq 2R_0$, the particle completes a full circle after detaching and resumes swimming to the right. In slightly narrower channels this can still occur, depending on the angle at which the bacterium exits the region where hydrodynamic forces disrupt circling. Peixin Zhang observed several such wall de- and reattachment events in the experiments as well. For clarity, a single representative trajectory from the simulations is shown in figure 4.31b.

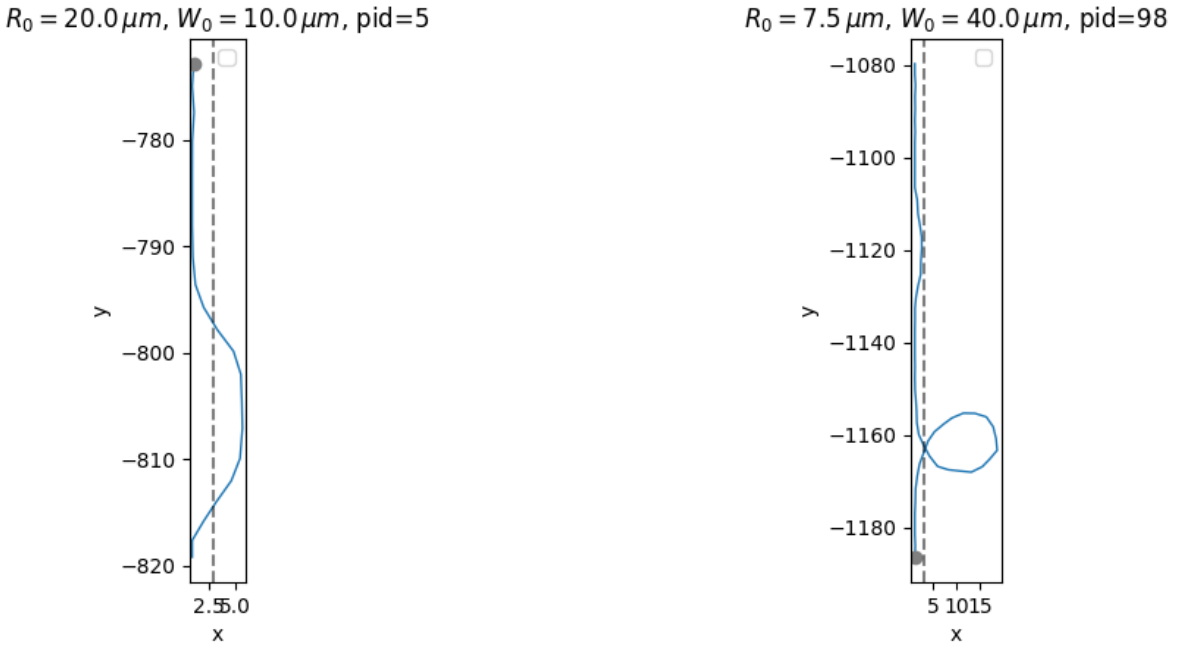

(a) Particle immediately reorienting back "left" after leaving a wall, and reattaching facing "left".

(b) Particle swimming "right", detaching, performing a full circle and reattaching still swimming "left".

Figure 4.31: Typical attachment events for same-side reattachments. Note that the scales are different in both plots, for better visibility.

4.9.2 Reattachment on other wall side

This is more likely in narrow channels, as the particle must traverse the full channel width after detachment. Under strong confinement, it occurs frequently. Note that for LR and RL, the absolute swimming direction in terms of Δy does not change. The directions in the symbols are defined relative to the bacterium's orientation with respect to the wall, so when the wall side changes, the bacterium's formal "swimming direction" is reversed.

Left to left - LL

This can only occur under strong confinement and strong diffusive effects, by coincidence. My criterion for whether a particle has moved "left" or "right" after initial attachment—namely the sign of Δy between the two events, depending on the wall side—may also create such events. It seems more likely here that a particle first moved left, then reoriented while still in the wall interaction region. It could then detach with a positive ϑ and reattach on the opposite wall side, just as a particle initially moving right would.

Left to right - LR

This occurs only under strong confinement. If a particle leaves the wall interaction region facing left and *immediately* diffuses into the opposite wall interaction region, this interaction can occur. It is shown in figure 4.32c.

Right to left - RL

This occurs mainly under strong and medium confinement. When a bacterium swims right, detaches, starts circling, and completes less than a quarter circle, this case arises. A typical trajectory is shown in figure 4.32b.

Right to right - RR

Under strong confinement, this event is extremely unlikely, since no particle has space to reorient more than half a circle. When the channel width satisfies $W_0 > \frac{1}{2}R_0$, however, it becomes the most likely case. A typical trajectory is shown in figure 4.32a.

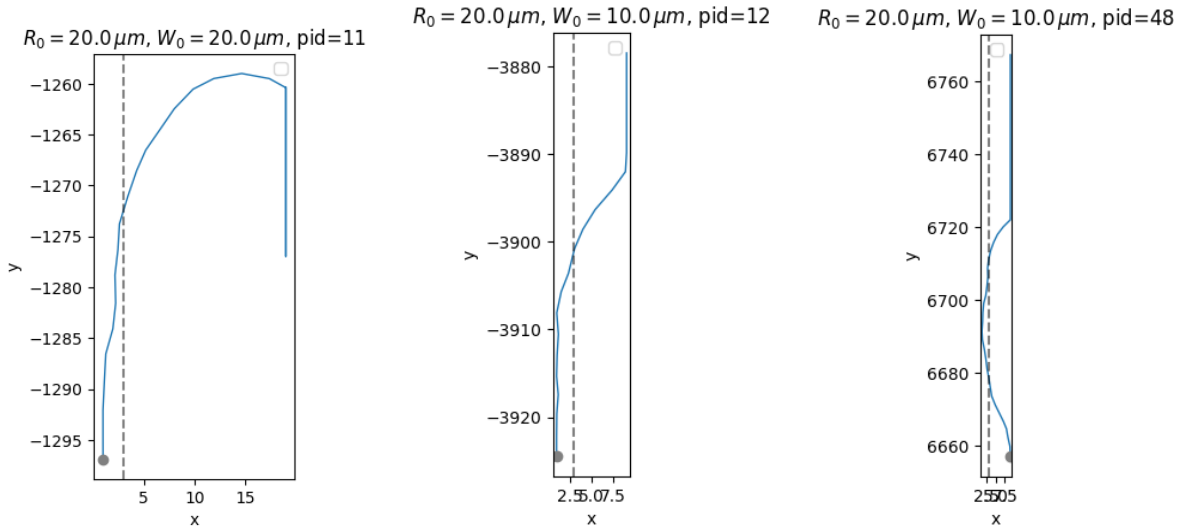

(a) Particle detaching swimming "right" and performing almost a full circle before reattaching on the other wall, still swimming "right".

(b) Particle detaching swimming "right" and reattaching on the other wall side swimming "left". This is even possible under mild confinement, since the swimmer "wants" to perform a full circular trajectory.

(c) Particle originally swimming "left" and then reattaching swimming "right". This is very rare and only possible under strong confinement and in narrow channels. Additionally, since the particle tends to reorient parallel to the opposite wall after detachment at a "left" swimming direction, it is very likely to detach again, as can be seen here.

Figure 4.32: Typical attachment events for opposite-side reattachments. Note that the scales are different in each plot, for better visibility.

4.9.3 Overview - De- and Reattachments

We now analyze the relative frequency of these events. First, in figure 4.33, we classify them into the two previously defined groups, depending on whether a particle crosses the channel between de- and reattachment.

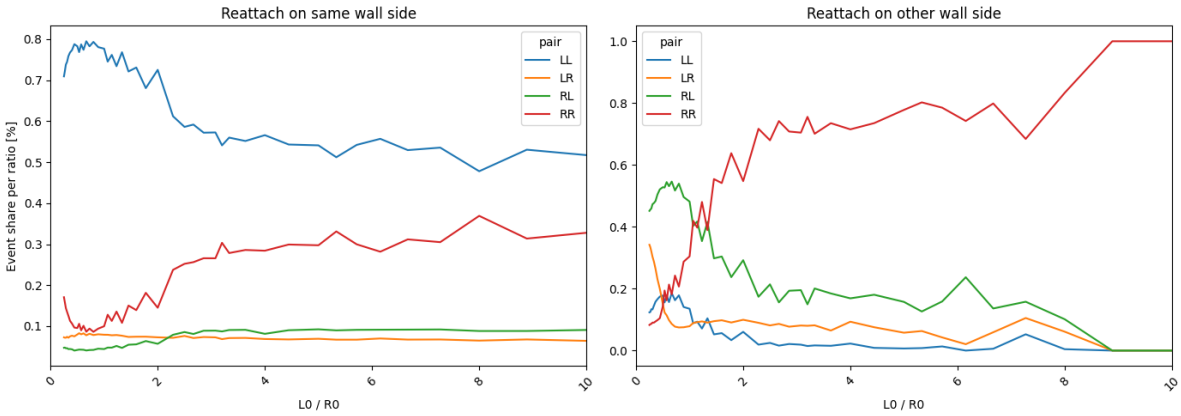

Figure 4.33: De- and Reattachment events, grouped by the classification if a particle crossed the channel after leaving a wall attachment region. Note that due to the huge amount of data, this plot is based on only on attachment events which eventually are going to detach from the wall again.

On the left, we see that regardless of confinement, circular swimming ensures a particle keeps moving left once it attaches to the left-facing wall. This effect is stronger under strong confinement but relevant in all geometries. Many recorded cases are statistical: some particles repeatedly jump in and out of the attachment region, sometimes dozens of times within short intervals. However, this could also occur for RR events, so the rotational preference clearly introduces a bias.

Under strong confinement, switching from right-swimming on one side to left-swimming on the other is much more likely than the reverse, especially when channels are just wide enough to allow a wall-force-free central region. This further strengthens the left-swimming bias in strong confinement.

For weak confinement, we observe almost no net flux. This is consistent with figure 4.15. Particles under weak confinement almost always retain their initial swimming direction. The dominance of RR events in the channel-crossing case arises simply because, after half a circle, the particle is *closest* to the opposite wall, i.e., its absolute swimming direction within the channel is effectively reversed. At this point, diffusion most likely causes attachment to the opposite wall. Considering the impact of these events on the total flux through the channel, it is also useful to look at their absolute frequencies. I plotted all events together in figure 4.34. We see that, relatively, channel-crossing events matter only for medium to strong confinement. Under strong confinement, bacteria are far more likely to start swimming left, and channel-crossing events that convert right-swimmers to left-swimmers—but not vice versa—further amplify this effect over longer observation times.

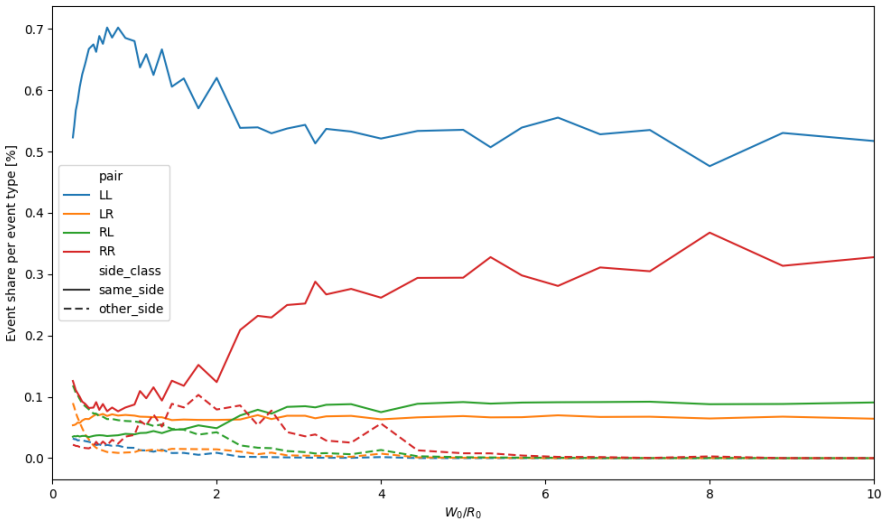

Figure 4.34: Combined events for same and other side de- and reattachment events. Note that due to the huge amount of data, this plot is based on only on attachment events which eventually are going to detach from the wall again.

5 Conclusion & Outlook

Bacterial hydrodynamics are highly complex, shaped by physiology, environment, flow, obstacles, fluctuations, and collective effects. While detailed models resolve individual flagella and collective motion, we explained the reversal of *E. coli* orientation preference under confinement using very simple computations.

Our key result is that purely geometrical, analytical arguments, shown in figure 4.26, explain significant parts of this behavior.

A major benefit of our approach is its reproducibility and adaptability. In experiments, small changes—such as diluting the bacterial suspension or redefining the “region" of incoming angles—strongly influenced the analysis. Clear, robust simulations clarified the mechanisms, allowing us to refine the experimental analysis for more meaningful and stable results.

We had planned (and implemented) Run & Tumble dynamics and wall-alignment torques, but restricting the model to basic geometric parameters provided clearer insight. This simplicity, combined with prior work by our Parisian colleagues and findings from previous research, now lets us predict how adding these effects would modify our results.

Including run-and-tumble dynamics would most likely add random noise and weaken our effects. We showed that bacteria *remaining* at walls and leaving only through random external forces are crucial for both directional preference and measurable fluxes. Thus, particles that remain attached to channel edges for extended periods of time dominate fluxes in confinement and narrow channels. This assumption agrees with Figuera-Morales et al. [34], who found that only a broad, power-law distribution of run times under flow allowed bacteria to move up channels: very long runs keep bacteria at walls longer, letting them travel farther. Since we effectively model only runs, and the experiments used smooth-swimming bacteria, shorter runs would reduce the observed effects.

The key qualitative difference between experiments and our simulations is *why* bacteria are “stuck" to the walls. In experiments, hydrodynamic interactions trap and align microswimmers parallel to the walls, so their velocity along the walls is nearly their propulsion speed, and they move quickly after attachment. In simulations, trapping is purely statistical: bacteria reach walls rapidly due to self-propulsion and remain there until they reorient. They stay longest when facing the wall; as their orientation diffuses away from the wall normal, they are more likely to leave, so the average velocity *at* the walls is lower. Adding a wall-alignment torque would likely increase the velocity parallel to the wall but might also accelerate diffusion away from the wall—an effect worth studying. However, any such torque would be largely estimated, since the *exact* dynamics are unclear and existing models often fail to match experiments.

We have shown that wall orientation preference under confinement is largely set by the geometry. It determines the probability of the initial attachment direction, which can reverse under strong confinement. For fixed channel width, the distribution of swimming radii is crucial, as the ratio of swimming radius to channel width controls orientation preference.

Many mechanisms remain unexplored: biofilms, epithelial attachment, complex surfaces; flow effects under specific conditions; and more precise fluid-dynamics models for flagella and other appendages. Collective locomotion in 2D and 3D is another key factor, actively studied by many groups.

A particularly interesting, and underexplored, question is *how* bacteria enter channels at all. Due to the symmetric nature of simulation results, it is logical to draw the conclusion that the asymmetry has to stem from bacterial history. Investigating the initial conditions and the way bacteria *enter* channels more closely could provide insights into the asymmetries observed in experiments.

Another promising next step is to refine the wall model. A more realistic setup would initialzse bacteria in a circular pool at the bottom of the channel and track how they spread as a function of swimming radius. Another is to introduce periodic patterns into the channel walls and study how their geometry and frequency affect swimming relative to the swimming radius.

6 Appendix

6.1 Data Management and workflows

Working with large datasets was one of the main things I had to learn during this thesis, so I briefly outline here how I dealt with the challenges that came up. In the beginning, I often struggled to reconstruct which code changes I had made for which parameter sets, which quickly became a serious problem for reproducibility and for keeping the analysis manageable. To address this, I developed a simple system for storing and loading data and metadata for each run.

Each code version now takes a '.json' parameter file as input. Besides all simulation, recording, and intra-run parameters, this file also contains a short, descriptive run title and a comment. After the simulation finishes, the parameter file is automatically extended with the simulation start date, the git commit hash, and the last commit message. This became especially important once different feature branches were introduced to represent various wall interaction models and bacterial kinematics.

To reduce RAM usage and increase simulation speed, data for each combination of W_0 and R_0 parameters is written to disk at the end of each run. Each dataset is stored in a parent folder named DDMMYY_simulation_title, with subfolders for event data frames, initial configuration snapshots, and statistics. The parameter file is saved in the parent folder, together with a separate Pandas DataFrame that collects file paths, run IDs, and metadata. The resulting file tree is shown in Figure 6.1.

```
Files/
‘-- DDMMYY_Simulation_Title/
    |-- events/
    |   ‘-- RunID_events.parquet
    |-- initial/
    |   |-- bins/
    |   |   ‘-- RunID_bins.npy
    |   |-- system_snapshots/
    |   |   ‘-- RunID_system.npy
    |   ‘-- trajectories/
    |       ‘-- RunID_paths.npy
    |-- steady/
    |   |-- bins/
    |   |   ‘-- RunID_bins.npy
    |   |-- system_snapshots/
    |   |   ‘-- RunID_system.npy
    |   ‘-- trajectories/
    |       ‘-- RunID_paths.npy
    |-- params_used.json
    |-- initial_conditions.npy
    ‘-- simulation_overview.parquet
```

Figure 6.1: Schematic file structure of the file organisation in this project.

The `simulation_overview.parquet` contains all the run metadata necessary for visual analysis, i.e. the R_0 and W_0 corresponding to each simulation `RunID`, with each file directory. Of course, if the data is loaded on a different machine than it was simulated on, the root directory has to be mapped, but otherwise the containing file paths are directly loadable. The structure is described in table 6.1:

Table 6.1: Overview table describing individual simulation runs and associated data files.

Column	Name	Symbol	Type	Unit	Description
1	run_id	r	int	–	Unique identifier of the simulation run
2	R0	R_0	float	μm	Initial radius of the surface or domain
3	L0	L_0	float	μm	Initial system length or box size
4	recording_start	t_{rec}	int	–	Timestep at which data recording starts
5	paths_file	–	string	–	Path to file containing particle trajectories
6	attachments_file	–	string	–	Path to file containing attachment/detachment events
7	bin_file	–	string	–	Path to binary file with binned or compressed data
8	system_file	–	string	–	Path to file containing system-level metadata

6.2 Selected code snippets

All code is available on GitHub upon request. The "standard" init function and the bacteria array is structured as follows:

```
def init(N, l):
# 0: x in ym
# 1: y in ym
# 2: phi in rad
# 3: is_attached flag
# 4: last_event_x
# 5: last_event_y
# 6: last_event_phi
# 7: last_event_t
# 8: last_event_type

arr = np.zeros((N, 9))

# initial state
arr[:, 0] = np.random.uniform(radius, l - radius, size=N)   #
    x
arr[:, 2] = np.random.uniform(0, 2*np.pi, size=N)           #
    phi

# initial attachment status from x
is_attached = (arr[:, 0] < attachment_region) | (arr[:, 0] >
   (l - attachment_region))
arr[:, 3] = is_attached.astype(int)

# no event yet
arr[:, 7] = -1   # no valid event start time yet
arr[:, 8] = -1   # no valid event type yet

return arr
```

The bacteria array is updated in the following manner:

```
def update(t, arr, l, omega):
was_attached = arr[:, 3] > 0
arr[:,0] += v0*np.cos(arr[:,2])*dt + np.sqrt(2*D_T*dt)*np.
   random.normal(size = (N))
arr[:,1] += v0*np.sin(arr[:,2])*dt + np.sqrt(2*D_T*dt)*np.
   random.normal(size = (N))

#check position validity
oob_left = arr[:,0] < radius
oob_right = arr[:,0] > (l - radius)
```

```
    #reset particles to wall
    arr[oob_left, 0] = radius + 10e-12
    arr[oob_right, 0] = 1 - radius - 10e-12

    #check where within eps
    within_epsilon_left = (arr[:,0] < epsilon)
    within_epsilon_right =  (arr[:,0] > (1-epsilon))

    #ORIENTATION UPDATES - general
    arr[:, 2] += np.sqrt(2*D_R*dt)*np.random.normal(size = (N))
    arr[~(within_epsilon_left|within_epsilon_right), 2] += omega*
       dt #within bulk with rotation
    arr[:, 2] = np.mod(arr[:, 2], 2*np.pi)


    #check where within attachment_region and update attachment
       status
    is_attached = (arr[:,0] < attachment_region) | (arr[:,0] > (1
       - attachment_region))
    arr[is_attached, 3] = 1
    arr[~is_attached, 3] = 0

    state_changed = was_attached != is_attached
    arr[state_changed, 4] = arr[state_changed, 0]    # x_start
    arr[state_changed, 5] = arr[state_changed, 1]    # y_start
    arr[state_changed, 6] = arr[state_changed, 2]    # phi_start
    arr[state_changed, 7] = t                       # t_start
    arr[state_changed & is_attached, 8] = 1         # attach
       event
    arr[state_changed & ~is_attached, 8] = 0        # detach
       event

    return arr
```

And the core "inner" loop is therefore:

```
                for t in range(math.floor(timesteps)):
                pos = bacteria.copy()
                update(t, bacteria, l, omega)

                #record attachments
                events = record_attachments(pos, bacteria, t)
                if events is not None:
                    event_list.append(events)

                # record trajectories
                if t % recording_interval == 0:
```

```
            # initial window
            if t < recording_duration:
                traj_record_initial[tii, :, :] = bacteria
                    [:recording_amount, :3]
                tii +=1

            # steady window
            elif t_steady <= t < t_steady +
                recording_duration:
                traj_record_steady[tis, :, :] = \
                    bacteria[:recording_amount, :3]
                tis +=1


        # binning / averaging
        if t < averaging_duration:
            calc_bins(bin_width, bins_initial, bacteria,
                pos)

        elif t_steady <= t < t_steady +
            averaging_duration:
            calc_bins(bin_width, bins_steady, bacteria,
                pos)

        # snapshot of steady-state system
        if t == t_steady:
            np.save(system_file_steady, bacteria)
```

6.3 Gridplots

As mentioned in the main part of the thesis, we usually started investigating the effect of a certain parameter by plotting a $R_{0,i} \times W_{0,i}$ grid over all simulation runs. I have attached a few of the more interesting ones here. Note that all of these were done with a slightly higher rate of rotational diffusion, at $D_R = 0.057\, rad^2/s$

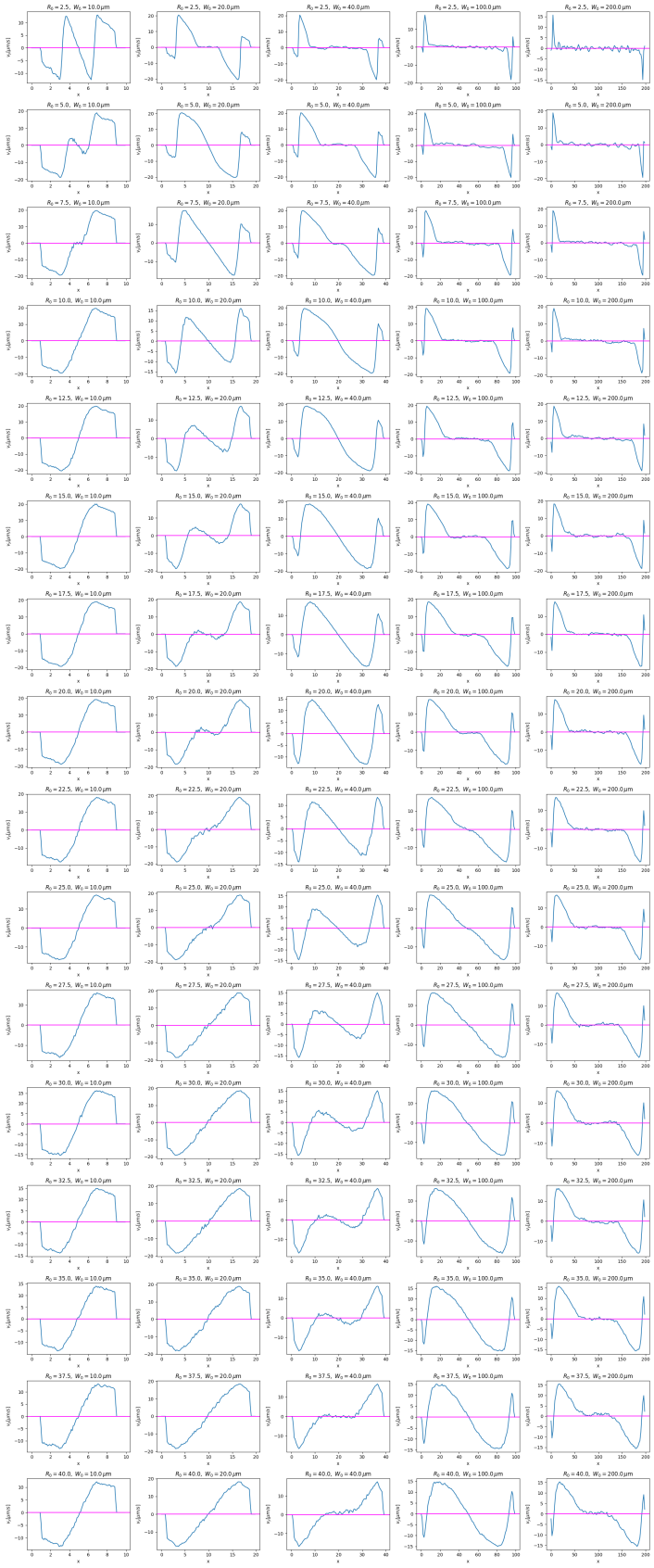

Figure 6.2: Grid showing all velocity bins over all simulation runs.

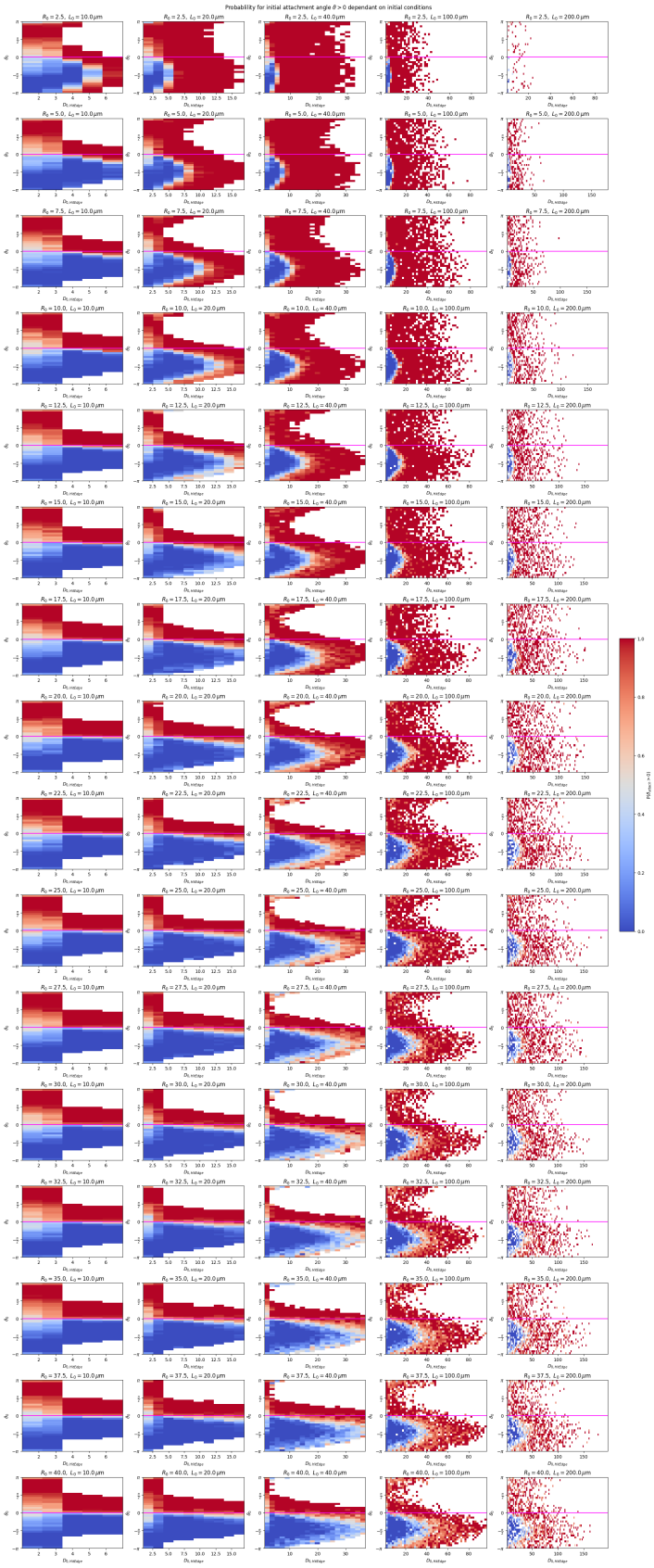

Figure 6.3: Grid showing the probability for a particle to swim left or right after attachment dependant on its initial conditions over all simulation runs.

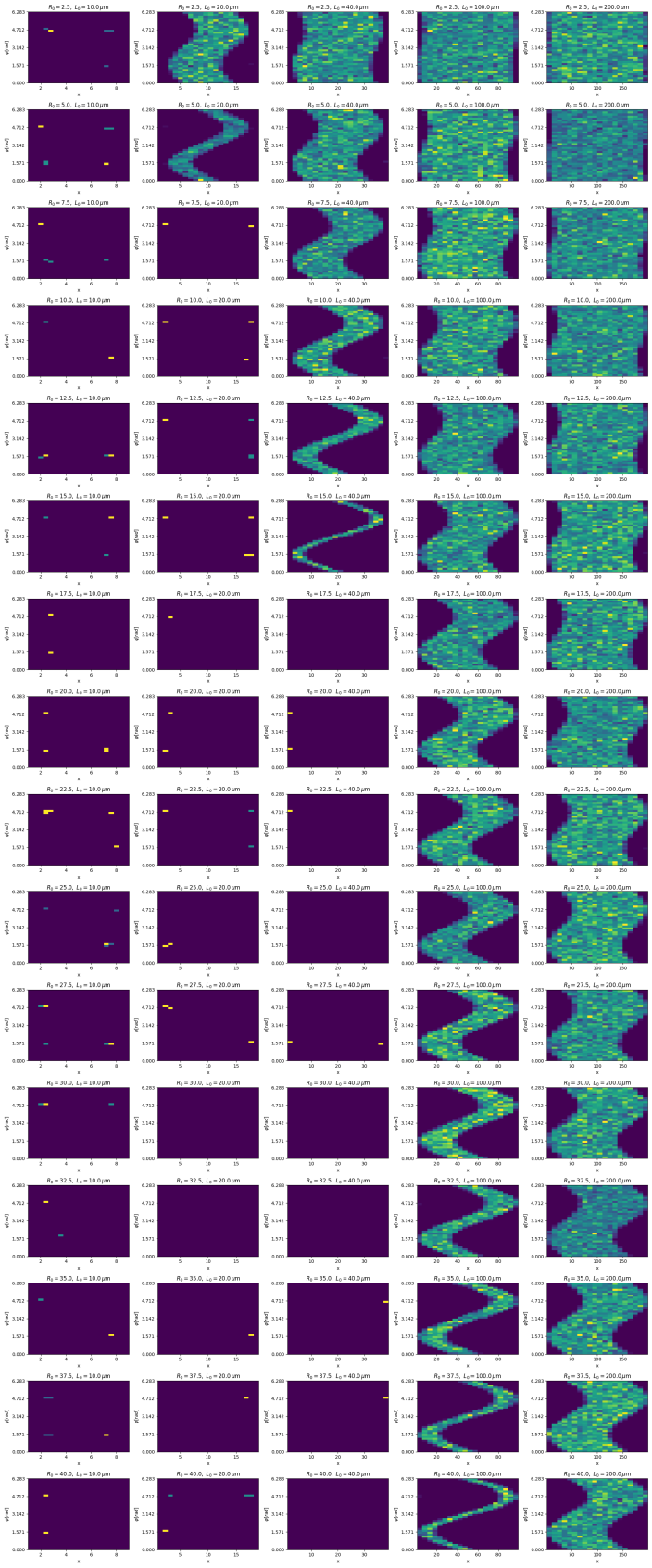

Figure 6.4: Grid showing the probability for a particle to never reach a wall and keep ccircling freely dependant on its initial conditions over all simulation runs.

6.4 Declaration of used tools

Tool	Purpose
Fortran	First iteration of the simulation code
Python / NumPy	Optimized second and final simulation code (vectorized)
pandas	Data exchange and processing
Matplotlib, Seaborn	Plotting and data analysis
ChatGPT	Assistance with plotting code and phrasing throughout the thesis
Writefull AI	Assistance with phrasing and language refinement
TexGPT	Assistance with LaTeX formatting
Mendeley	Literature management and citation workflow

Table 6.2: Software tools and AI assistants used during this work

List of Figures

List of Tables

Bibliography

[1] Ewen Callaway. These are the 20 most-studied bacteria - the majority have been ignored. *Nature*, 637(8047):770–771, 1 2025. ISSN 14764687. doi: 10.1038/D41586-025-00038-X;SUBJMETA.

[2] World Health Organisation. E. coli, 2026. URL `https://www.who.int/news-room/fact-sheets/detail/e-coli`.

[3] Zachary D. Blount. The unexhausted potential of E. coli. *eLife*, 2015(4), 3 2015. ISSN 2050084X. doi: 10.7554/ELIFE.05826.

[4] Amie R. Tuttle, Nicholas D. Trahan, and Mike S. Son. Growth and Maintenance of Escherichia coli Laboratory Strains. *Current protocols*, 1(1):e20, 1 2021. ISSN 26911299. doi: 10.1002/CPZ1.20. URL `https://pmc.ncbi.nlm.nih.gov/articles/PMC8006063/`.

[5] James B. Kaper, James P. Nataro, and Harry L.T. Mobley. Pathogenic Escherichia coli. *Nature Reviews Microbiology 2004 2:2*, 2(2):123–140, 2 2004. ISSN 1740-1534. doi: 10.1038/nrmicro818. URL `https://www.nature.com/articles/nrmicro818`.

[6] Walter E. Stamm and S. Ragnar Norrby. Urinary tract infections: Disease panorama and challenges. *Journal of Infectious Diseases*, 183:S1–S4, 3 2001. ISSN 00221899. doi: 10.1086/318850.

[7] Ana L. Flores-Mireles, Jennifer N. Walker, Michael Caparon, and Scott J. Hultgren. Urinary tract infections: epidemiology, mechanisms of infection and treatment options. *Nature reviews. Microbiology*, 13(5):269, 5 2015. ISSN 17401534. doi: 10.1038/NRMICRO3432. URL `https://pmc.ncbi.nlm.nih.gov/articles/PMC4457377/`.

[8] Shane Whelan, Brigid Lucey, and Karen Finn. Uropathogenic Escherichia coli (UPEC)-Associated Urinary Tract Infections: The Molecular Basis for Challenges to Effective Treatment. *Microorganisms*, 11(9):2169, 9 2023. ISSN 20762607. doi: 10.3390/MICROORGANISMS11092169. URL `https://pmc.ncbi.nlm.nih.gov/articles/PMC10537683/`.

[9] Betsy Foxman. Urinary tract infection syndromes. Occurrence, recurrence, bacteriology, risk factors, and disease burden. *Infectious Disease Clinics of North America*, 28(1):1–13, 3 2014. ISSN 08915520. doi: 10.1016/j.idc.2013.09.003. URL `https://pubmed.ncbi.nlm.nih.gov/24484571/`.

[10] Andreas Reisner, Mario Maierl, Michael Jörger, Robert Krause, Daniela Berger, Andrea Haid, Dijana Tesic, and Ellen L. Zechner. Type 1 fimbriae contribute to catheter-associated urinary tract infections caused by Escherichia coli. *Journal of Bacteriology*, 196

(5):931–939, 3 2014. ISSN 00219193. doi: 10.1128/JB.00985-13/ASSET/F32D22CB-17AB-49F0-9B94-6FF97D239E8B/ASSETS/GRAPHIC/ZJB9990930400005.JPEG. URL https://journals.asm.org/journal/jb.

[11] G. J. Sibona. Evolution of microorganism locomotion induced by starvation. *Physical Review E*, 76(1):011919, 7 2007. ISSN 15393755. doi: 10.1103/PhysRevE.76.011919. URL https://journals.aps.org/pre/abstract/10.1103/PhysRevE.76.011919.

[12] Eric Lauga. Bacterial Hydrodynamics. *Annual Review of Fluid Mechanics*, 48:105–130, 1 2016. ISSN 00664189. doi: 10.1146/annurev-fluid-122414-034606.

[13] Jens Elgeti and Gerhard Gompper. Wall accumulation of self-propelled spheres. *EPL*, 101 (4), 2 2013. ISSN 02955075. doi: 10.1209/0295-5075/101/48003.

[14] Eric Lauga, Willow R. DiLuzio, George M. Whitesides, and Howard A. Stone. Swimming in circles: Motion of bacteria near solid boundaries. *Biophysical Journal*, 90(2):400–412, 2006. ISSN 00063495. doi: 10.1529/biophysj.105.069401.

[15] Willow R. DiLuzio, Linda Turner, Michael Mayer, Piotr Garstecki, Douglas B. Weibel, Howard C. Berg, and George M. Whitesides. Escherichia coli swim on the right-hand side. *Nature*, 435 (7046):1271–1274, 6 2005. ISSN 00280836. doi: 10.1038/nature03660.

[16] Keiji Tanaka and Koichi Shimakawa. Structure. *Amorphous Chalcogenide Semiconductors and Related Materials*, pages 31–65, 7 1996. doi: 10.1007/978-3-030-69598-9_2. URL https://www.ncbi.nlm.nih.gov/books/NBK8477/.

[17] Junio Oliveira and Wanda C. Reygaert. Gram-Negative Bacteria. *Infection Management for Geriatrics in Long-Term Care Facilities, Second Edition*, pages 427–443, 8 2023. doi: 10.1385/1-59259-036-5:43. URL https://www.ncbi.nlm.nih.gov/books/NBK538213/.

[18] Howar Berg. *E. coli in motion*. Springer, New York, NY, Cambridge, MA, 2004. ISBN 0-378-00888-8. doi: 10.1007/978-0-387-21638-6_12. URL https://link.springer.com/chapter/10.1007/978-0-387-21638-6$_1$2.

[19] Michael Eisenbach. Bacterial Chemotaxis. *Encyclopedia of Life Sciences*, 4 2001. doi: 10.1038/NPG.ELS.0001251. URL https://www.researchgate.net/publication/228050570$_B acterial_C hemotaxis$.

[20] E. M. Purcell. lowreynolds. Technical report, Harvard University, Cambridge, 6 1976.

[21] Kai Zhao, Mingzhu Liu, and Richard R. Burgess. Adaptation in bacterial flagellar and motility systems: from regulon members to 'foraging'-like behavior in E. coli. *Nucleic Acids Research*, 35(13):4441–4452, 7 2007. ISSN 0305-1048. doi: 10.1093/NAR/GKM456. URL https://dx.doi.org/10.1093/nar/gkm456.

[22] Howard C. Berg. The rotary motor of bacterial flagella. *Annual Review of Biochemistry*, 72: 19–54, 2003. ISSN 00664154. doi: 10.1146/ANNUREV.BIOCHEM.72.121801.161737.

[23] Navish Wadhwa and Howard C. Berg. Bacterial motility: machinery and mechanisms. *Nature Reviews Microbiology 2021 20:3*, 20(3):161–173, 9 2021. ISSN 1740-1534. doi: 10.1038/s41579-021-00626-4. URL https://www.nature.com/articles/s41579-021-00626-4.

[24] Nicholas C. Darnton, Linda Turner, Svetlana Rojevsky, and Howard C. Berg. On torque and tumbling in swimming Escherichia coli. *Journal of bacteriology*, 189 (5):1756–1764, 3 2007. ISSN 0021-9193. doi: 10.1128/JB.01501-06. URL https://pubmed.ncbi.nlm.nih.gov/17189361/.

[25] Eric Lauga and Thomas R. Powers. The hydrodynamics of swimming microorganisms. *Rep. Prog. Phys.*, 72(9):096601, 2009. ISSN 00344885. doi: 10.1088/0034-4885/72/9/096601.

[26] Ken F. Jarrell and Mark J. McBride. The surprisingly diverse ways that prokaryotes move, 6 2008. ISSN 17401526.

[27] Johannes M. Keegstra, Francesco Carrara, and Roman Stocker. The ecological roles of bacterial chemotaxis. *Nature Reviews Microbiology 2022 20:8*, 20(8): 491–504, 3 2022. ISSN 1740-1534. doi: 10.1038/s41579-022-00709-w. URL https://www.nature.com/articles/s41579-022-00709-w.

[28] Roshni Bano, Patrick Mears, Ido Golding, and Yann R. Chemla. Flagellar dynamics reveal fluctuations and kinetic limit in the Escherichia coli chemotaxis network. *Scientific Reports 2023 13:1*, 13(1):22891–, 12 2023. ISSN 2045-2322. doi: 10.1038/s41598-023-49784-w. URL https://www.nature.com/articles/s41598-023-49784-w.

[29] Bohan Wu-Zhang, Peixin Zhang, Renaud Baillou, Anke Lindner, Eric Clement, Gerhard Gompper, and Dmitry A. Fedosov. Run-and-tumble dynamics of Escherichia coli is governed by its mechanical properties. *Journal of the Royal Society Interface*, 22(227), 6 2025. ISSN 17425662. doi: 10.1098/RSIF.2025.0035/235931. URL https://dx.doi.org/10.1098/rsif.2025.0035.

[30] R. M. Macnab. Bacterial flagella rotating in bundles: a study in helical geometry. *Proceedings of the National Academy of Sciences*, 74(1):221–225, 1 1977. ISSN 00278424. doi: 10.1073/PNAS.74.1.221. URL https://www.pnas.org/doi/abs/10.1073/pnas.74.1.221.

[31] P. Romanczuk, M. Bär, W. Ebeling, B. Lindner, and L. Schimansky-Geier. Active Brownian particles: From individual to collective stochastic dynamics: From individual to collective stochastic dynamics, 3 2012. ISSN 19516355.

[32] Linda Turner, William S. Ryu, and Howard C. Berg. Real-time imaging of fluorescent flagellar filaments. *Journal of Bacteriology*, 182(10):2793–2801, 5 2000. ISSN 00219193. doi: 10.1128/JB.182.10.2793-2801.2000. URL https://www.researchgate.net/publication/12534320$_{R}eal-Time_{I}maging_{o}f_{F}luorescent_{F}lagellar_{F}ilaments$.

[33] Ekaterina Korobkova, Thierry Emonet, Jose M.G. Vilar, Thomas S. Shimizu, and Philippe Cluzel. From molecular noise to behavioural variability in a single bacterium. *Nature 2004 428:6982*, 428(6982):574–578, 4 2004. ISSN 1476-4687. doi: 10.1038/nature02404. URL `https://www.nature.com/articles/nature02404`.

[34] Nuris Figueroa-Morales, Aramis Rivera, Rodrigo Soto, Anke Lindner, Ernesto Altshuler, and Éric Clément. E. Coli "super-contaminates" narrow ducts fostered by broad run-time distribution. *Science Advances*, 6(11):155–168, 2020. ISSN 23752548. doi: 10.1126/SCIADV.AAY0155/ASSET/139168D1-C9ED-4869-AEB7-77541AB325F6/ASSETS/GRAPHIC/AAY0155-F6.JPEG. URL `https://www.science.org`.

[35] Joseph Feher. Physical Foundations of Physiology I. *Quantitative Human Physiology*, pages 15–30, 2017. doi: 10.1016/B978-0-12-800883-6.00002-1.

[36] Suddhashil Chattopadhyay, Radu Moldovan, Chuck Yeung, and X. L. Wu. Swimming efficiency of bacterium Escherichia coli. *Proceedings of the National Academy of Sciences of the United States of America*, 103(37):13712–13717, 9 2006. ISSN 00278424. doi: 10.1073/PNAS.0602043103;SUBPAGE:STRING:FULL. URL `/doi/pdf/10.1073/pnas.0602043103?download=true`.

[37] Knut Drescher, Jörn Dunkel, Luis H Cisneros, Sujoy Ganguly, Raymond E Goldstein, R E G Designed, and R E G Performed. Fluid dynamics and noise in bacterial cell-cell and cell-surface scattering. doi: 10.1073/pnas.1019079108/-/DCSupplemental.

[38] Silvio Bianchi, Filippo Saglimbeni, and Roberto Di Leonardo. Holographic imaging reveals the mechanism of wall entrapment in swimming bacteria. *Physical Review X*, 7(1), 1 2017. ISSN 21603308. doi: 10.1103/PhysRevX.7.011010.

[39] Paolo Sartori, Enrico Chiarello, Gaurav Jayaswal, Matteo Pierno, Giampaolo Mistura, Paola Brun, Adriano Tiribocchi, and Enzo Orlandini. Wall accumulation of bacteria with different motility patterns. *PHYSICAL REVIEW E*, 97:22610, 2018. doi: 10.1103/PhysRevE.97.022610.

[40] Allison P. Berke, Linda Turner, Howard C. Berg, and Eric Lauga. Hydrodynamic attraction of swimming microorganisms by surfaces. *Physical Review Letters*, 101(3), 7 2008. ISSN 00319007. doi: 10.1103/PHYSREVLETT.101.038102. URL `http://arxiv.org/abs/0806.2898` `http://dx.doi.org/10.1103/PhysRevLett.101.038102`.

[41] Rothschild. Rothschild - 1963 - Non-random distribution of bull spermatozoa in a drop of sperm suspension. *NATURE*, pages 1221–1222, 6 1964.

[42] Selma Maria Köhler. "Long-term movement of chiral microswimmers in confined spaces" verfasst von / submitted by. Technical report.

[43] Konstantin Schaar, Andreas Zöttl, and Holger Stark. Detention Times of Microswimmers Close to Surfaces: Influence of Hydrodynamic Interactions and Noise. *Physical Review Letters*, 115(3), 7 2015. ISSN 10797114. doi: 10.1103/PhysRevLett.115.038101.

[44] Guanglai Li and Jay X. Tang. Accumulation of microswimmers near a surface mediated by collision and rotational Brownian motion. *Physical Review Letters*, 103(7), 8 2009. ISSN 00319007. doi: 10.1103/PhysRevLett.103.078101.

[45] Brownian Agents and Active F Particles Schweitzer. Book Review: Brownian Agents and Active Particles. Technical Report 2, 2004.

[46] Andreas Zöttl and Holger Stark. Emergent behavior in active colloids, 5 2016. ISSN 1361648X.

[47] Francesco Giorgi, Judith M. Curran, and Eann A. Patterson. Real-time monitoring of the dynamics and interactions of bacteria and the early-stage formation of biofilms. *Scientific Reports 2022 12:1*, 12(1):18146–, 10 2022. ISSN 2045-2322. doi: 10.1038/s41598-022-22669-0. URL `https://www.nature.com/articles/s41598-022-22669-0`.

[48] K. Ledwoch, S. J. Dancer, J. A. Otter, K. Kerr, D. Roposte, L. Rushton, R. Weiser, E. Mahenthiralingam, D. D. Muir, and J. Y. Maillard. Beware biofilm! Dry biofilms containing bacterial pathogens on multiple healthcare surfaces; a multi-centre study. *Journal of Hospital Infection*, 100(3):e47–e56, 11 2018. ISSN 0195-6701. doi: 10.1016/J.JHIN.2018.06.028.

[49] Karen Ejrnaes. Bacterial Characteristics of Importance for Recurrent Urinary Tract Infections Caused by Escherichia coli. *J. Clin. Microbiol*, 58(4):1776–1781, 2011.

[50] Alexandre Persat, Carey D. Nadell, Minyoung Kevin Kim, Francois Ingremeau, Albert Siryaporn, Knut Drescher, Ned S. Wingreen, Bonnie L. Bassler, Zemer Gitai, and Howard A. Stone. The Mechanical World of Bacteria. *Cell*, 161(5):988–997, 5 2015. ISSN 0092-8674. doi: 10.1016/J.CELL.2015.05.005.

[51] Andreas Zöttl. Hydrodynamics of Microswimmers in Confinement and in Poiseuille Flow. Technical report, 2014.